Chemical and optical properties of marine boundary layer aerosol particles of the mid-Pacific in relation to sources and meteorological transport

P. K. Quinn, V. N. Kapustin,[1] and T. S. Bates[1]

NOAA, Pacific Marine Environmental Laboratory, Seattle, Washington

D. S. Covert[1]

Department of Atmospheric Sciences, University of Washington, Seattle

Abstract. Incorporating the direct effect of tropospheric aerosol on climate into global climate models involves coupling the optical properties of the aerosol with its physical and chemical properties. This coupling is strengthened if the optical, physical, and chemical properties of the individual aerosol components are known as well as how these properties depend on the air mass source and synoptic scale meteorology. To relate properties of the aerosol components to air mass sources over a wide range of meteorological conditions, two long latitudinal cruises were conducted in the central Pacific Ocean from 55°N to 70°S. Submicron non-sea-salt (nss) $SO_4^=$ aerosol averaged about 35 to 40% of the submicron ionic mass as analyzed by ion chromatography and 6% of the total ionic mass, while supermicron nss $SO_4^=$ aerosol contributed about 1% to the total ionic mass. About 1% of the remaining total ionic mass was composed of methanesulfonate and 90% was sea salt. Ionic mass fractions of nss $SO_4^=$ aerosol were highest in regions having the longest marine boundary layer residence times or the largest source of marine or continental gas phase precursors. The calculated scattering by nss $SO_4^=$ aerosol was highest in these same regions due to the dependence of scattering on particle size and the concentration of nss $SO_4^=$ in the submicron size range. The calculated scattering by submicron sea salt was similar to that of the nss $SO_4^=$ aerosol, indicating that its contribution to scattering in the marine boundary layer can be significant or even dominant depending on its mass concentration. Mass scattering efficiencies for nss $SO_4^=$ at 30% RH ranged from 4.3 to 7.5 $m^2 g^{-1}$ and for submicron sea salt from 3.5 to 7.7 $m^2 g^{-1}$. Mass backscattering efficiencies for nss $SO_4^=$ ranged from 0.41 to 0.58 $m^2 g^{-1}$ and for submicron sea salt from 0.33 to 0.63 $m^2 g^{-1}$. These values fall within the same range as others reported previously for the marine atmosphere.

1. Introduction

The direct effect of tropospheric aerosol on climate results from the scattering by particles of incoming shortwave radiation with a portion of it being reflected back to space. Defining climate forcing as an externally imposed change on the Earth's heat balance implies that a knowledge of the radiative properties of both natural and anthropogenic aerosol components are needed to calculate any change in the reflected flux, ΔF_R, due to an anthropogenic perturbation in aerosol loading or optical properties. Parameters needed to calculate ΔF_R include the mass concentration of each aerosol chemical component, the mass scattering efficiency, or the light scattering efficiency per unit mass of each aerosol component j, $\alpha_{sp,j}$, and the fraction of scattered light that is directed upward, β. The latter quantity can be approximated through the measurement of the backscattered

fraction, b, which is the fraction of scattered light that is redirected to the backward hemisphere of the particle. Consideration of b is useful as many values have been reported for a variety of air mass types. The quantities b and β are equal for a zenith Sun angle.

The dominant aerosol components present in the marine boundary layer include nss $SO_4^=$ aerosol, sea-salt aerosol, mineral dust, organic carbon species, and to a lesser extent, elemental carbon. In general, a component is composed of several chemical elements, compounds, or ions. Non-sea-salt $SO_4^=$ aerosol found in the marine boundary layer can have marine, volcanic, and anthropogenic sources. Therefore it can be part of the natural aerosol system or it can be an anthropogenic perturbation of that system such that it will contribute to climate forcing by tropospheric aerosol. It may be derived from the oxidation of biogenic dimethylsulfide (DMS) which is emitted from the ocean surface [*Andreae*, 1986; *Bates et al.*, 1987], the oxidation of volcanic gas phase SO_2 [*Stoiber et al.*, 1987], or the long range transport of anthropogenic air masses from continental regions [*Quinn et al.*, 1990]. The latter may involve transport through the free troposphere [*Clarke*, 1993]. Impactor measurements indicate that nss $SO_4^=$ aerosol mass is concentrated primarily in the 0.1 to 1.0 µm diameter size range [e.g., *Whitby*,

---

[1]Also at Joint Institute for the Study of the Atmosphere and Ocean, University of Washington, Seattle.

1978; *Savoie and Prospero,* 1982; *Pszenny et al.,* 1989; *Quinn et al.,* 1993].

Sea-salt aerosol is derived from the evaporation of seaspray droplets and hence is part of the natural marine aerosol system. It dominates the mass of the supermicron particle size range in the marine boundary layer but can also contribute a significant amount of mass to the submicron size range [*O'Dowd and Smith,* 1993]. The number concentration of sea-salt aerosol in the submicron size range is small, however, often contributing only 4 to 10% of the total number [*McInnes et al.,* 1995a].

Particles containing mineral dust are produced by the weathering of soils and rock as well as through industrial and agricultural practices. These particles have diameters ranging from less than 1 μm to 100 μm. Those with diameters up to about 4 μm can be transported over long distances [*Merrill et al.,* 1994], so that at times they can contribute a significant amount of mass to the marine boundary layer aerosol.

Organic carbon compounds in the marine boundary layer can have natural marine and terrestrial sources as well as anthropogenic sources. The ocean is a source of particulate organic species through the direct injection of biogenic surfactants from bubble bursting processes [*Monahan,* 1986] or the emission of gas phase precursors [*Plass-Dulmer et al.,* 1995]. Gaseous organic carbon species emitted by natural terrestrial sources and anthropogenic combustion may be transformed to the aerosol phase through oxidation or condensation and transported over long distances to the marine atmosphere. To date, the organic content of marine aerosol particles has not been well quantified or speciated. The few data that have been reported indicate that carbon-containing species can make up 4 to 15% of the total marine aerosol mass with more than 90% of this mass in the form of organic carbon [*Rau and Khalil,* 1993].

From the number-size distribution and an estimation of the particle density and refractive index, the scattering and backscattering coefficients, σ_{sp} and σ_{bsp}, can be calculated for the total aerosol with Mie theory. In addition, knowledge of the chemical mass-size distribution of each aerosol component j allows for the calculation of the scattering coefficient of that component, or $\sigma_{sp,j}$. The scattering coefficient for the components then can be used to determine the fractional contribution of the component to scattering and backscattering by the aerosol as a whole and to calculate the mass scattering efficiency of the component. For aerosol component j the mass scattering efficiency is defined as the component's scattering increment per mass increment or

$$\alpha_{sp,j} = \frac{\partial \sigma_{sp,j}}{\partial m_j}. \qquad (1)$$

If the total mass of component j is not known, an individual species can be used as an indicator for that component. For example, the nss $SO_4^=$ ion can be used as an indicator to represent the complete nss $SO_4^=$ aerosol component composed of nss $SO_4^=$ and the mass of NH_4^+ and H_2O that is universally associated with it under most atmospheric conditions.

The magnitude of the scattering and backscattering coefficients of each aerosol component depends on its size dependent mass (or volume) concentration. The dependence of the scattering coefficient on particle size is shown in Figure 1 for a wavelength of 0.55 μm, particles of unit volume, and a refractive index of $1.5-10^{-7}i$, which is near that of $(NH_4)_2SO_4$ and sea salt at low relative humidity. For these conditions, on a mass or volume basis, the scattering efficiency is lognormally distributed with the most efficient size range for scattering occurring between particle diameters of 0.2 and 1.0 μm.

What this implies for scattering by atmospheric aerosols is shown by comparing these calculated scattering efficiency size distributions with size distributions of the atmospheric aerosol. Figure 1 shows two measured size distributions, one from a marine air mass (solid line with symbols) and one from a continentally influenced air mass (dashed line with symbols). For the marine case, the minimum between the submicron and supermicron modes coincides with the maximum in the scattering distribution. Therefore scattering by the total aerosol will be affected by both modes but largely controlled by the supermicron mode due to its large mass concentration, in spite of the decrease in the scattering coefficient with size. For the continental case, the submicron mode will have a larger effect on scattering by the aerosol as a whole than it did in the marine case, as its peak diameter is shifted toward the maximum in the scattering distribution. The supermicron mode will have a smaller effect, however, as it has a lower mass concentration. Clearly, both the geometric volume mean diameter and the mass concentration of an atmospheric aerosol component will strongly affect the amount the component contributes to scattering by the whole aerosol.

For a given aerosol mass concentration and number distribution, differences in chemical composition also will affect scattering by the total aerosol. This effect is such that for diameters between 0.2 and 0.3 μm, an increase in the real portion of the refractive index from 1.4 (50% H_2SO_4 / 50% H_2O) to 1.5 (($NH_4)_2SO_4$) yields a 60% increase in σ_{sp} and a 50% increase in σ_{bsp} [*Marshall,* 1994]. As a result, the degree of neutralization of nss $SO_4^=$ aerosol by NH_3 (g) will affect scattering by the total aerosol. Similarly, the addition of a significant amount of sea salt, which also has a refractive index near 1.5, to a H_2SO_4 aerosol also will affect scattering by the total aerosol. The backscattered fraction shows the largest sensitivity to change in refractive index at a diameter near 1.0 μm [*Marshall,* 1994]. Hence b will change with wind speed as the mass distribution of sea-salt aerosol changes above and below 1.0 μm. The optical properties of the aerosol also will be affected by the incorporation of a small amount of a strong absorber such as elemental carbon. Such changes have yet to be quantified, however.

As indicated in the above discussion, the size dependent chemical composition and mass concentration of tropospheric aerosol components determine the optical properties of the aerosol. These size dependent aerosol parameters are, in turn, a result of synoptic scale meteorology and air mass sources. Data collected during two Radiatively Important Trace Species (RITS) cruises in the central Pacific Ocean have allowed for an analysis of the effect of meteorological transport on the number distribution [*Covert et al.,* 1995]. The number concentration in the Aitken (particle diameter, D_p, of 0.01 to 0.1 μm) and accumulation (D_p of 0.1 to 0.5 μm) modes was found to depend on the relative importance of the transport of ultrafine (<0.01 μm) and Aitken particles from the free troposphere to the marine boundary layer versus the aging of Aitken and accumulation mode particles within the boundary layer due to vapor condensation and cloud processing. In middle- and high-latitude regions, subsidence from the free troposphere was frequent and aging processes were limited by the short amount of time the aerosol spent in the boundary layer. As a result, the Aitken mode dominated the number distribution but contributed little to total mass or light scattering. In the tropics, more time in the boundary layer and more frequent clouds led to size distributions with roughly equal number in the Aitken and accumulation modes and, accordingly, a greater mass in the accumulation mode.
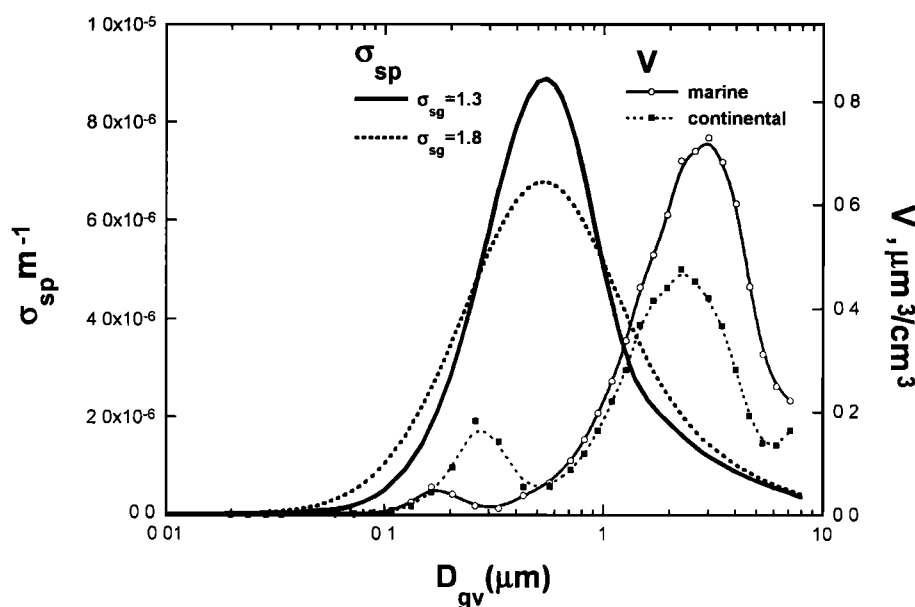
Parameter	Marine		Continental	
	accumulation mode	coarse model	accumulation mode	coarse mode
V, μm^3 cm^{-3}	0.14	7.34	0.49	4.82
D_{gv}, μm	0.197	2.72	0.295	2.43
σ_{sg}	1.31	1.82	1.33	1.82

Figure 1. Plain solid and dashed lines represent the scattering coefficient as a function of geometric mean volume diameter, D_{gv}, estimated from a Mie calculation using a wavelength of 0.55 μm, a particle refractive index of 1.5–10^{-7}i, and a total particle volume of 1 μm^3 cm^{-3}. The calculation was done for geometric standard deviations, σ_{sg}, of 1.3 and 1.8. Solid and dashed lines with symbols represent volume concentrations as a function of D_{gv} calculated from measured number-size distributions during one of the Radiatively Important Trace Species (RITS 93) cruises. These size distributions are averages over impactor samples collected in marine (solid line, 2°N) and continental (dashed line, 27°N) air masses. DISTFIT (version 1.10, TSI) was used to calculate the modal parameters.

A similar data analysis of meteorology and aerosol chemistry should reveal the effect of air mass sources and meteorological transport on the relative concentrations and mass distributions of the individual aerosol components. Therefore the same two RITS data sets have been analyzed to define the relationship between aerosol optical properties and source-determined chemical properties. The RITS 93 cruise traveled from 70°S to 55°N along 140°W from March to May 1993 (Figure 2a). The RITS 94 cruise (Figure 2b) followed the same track but in the opposite direction from November 1993 to January 1994. Presented here are the results from these data sets which (1) relate synoptic scale meteorology and air mass sources to aerosol size dependent chemical composition in the marine boundary layer, (2) define the mass fraction of each aerosol ionic component present, (3) relate the ionic mass fraction of each aerosol component to its contribution to scattering and backscattering by the aerosol as a whole, and (4) determine the mass scattering efficiency for the ionic aerosol components. In addition, these results are compared to those reported from previous studies of marine air masses.

2. Methods

2.1. Measurements

The RITS 93 and RITS 94 cruise tracks are shown in Figures 2a and 2b, respectively. Sample air for all measurements was drawn through a 6-m heated sample inlet and dried to a relative humidity (RH) near 30%. The top of the inlet was 18 m above the ocean surface and 10 m forward of the ship's stack.

The number distribution between 0.02 and 0.6 μm was measured every 10 min with a differential mobility analyzer (DMA) (TSI model 3071 [*Liu and Pui*, 1975]) in conjunction with a condensation particle counter (CPC) (TSI model 3760). A Kr 85 charge neutralizer (TSI model 3077) was used to produce an equilibrium charge distribution. An impactor with a 50% cutoff diameter of 0.7 μm bounded the upper limit of the aerosol at the inlet and facilitated the inversion algorithm. A minimum of 1000 particles was counted in each size increment, yielding an uncertainty of about 3% for one standard deviation, assuming Poisson counting statistics. The number concentration was corrected for the counting efficiency of the particle counter [*Zang and Liu*, 1991] and diffusion losses in the DMA [*Reineking and Porstendorfer*, 1986]. A Boltzmann-Fuchs equilibrium charge distribution was assumed to be present on the particles analyzed. The number-mobility distribution was inverted to a number-size distribution using an algorithm similar to that provided by the manufacturer [*Keady et al.*, 1983].

The number distribution between 0.6 and 9.6 μm was measured with an aerodynamic particle sizer (APS) (TSI model 3300 [*Baron*, 1986]). The calibration of the APS was checked between cruises with polystyrene latex spheres and found to be within 1% of the manufacturer's calibration. The APS was
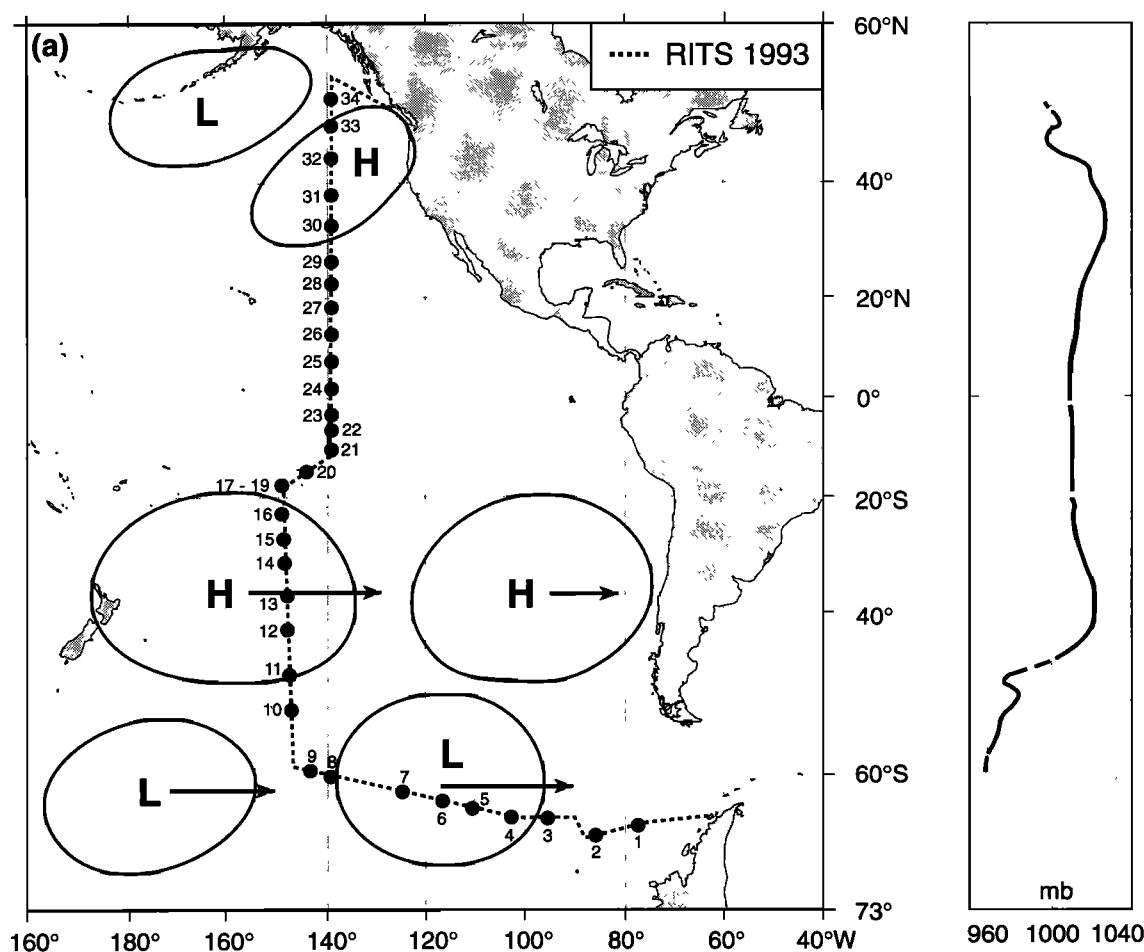
Figure 2. Composite surface synoptic maps of the Pacific for (a) RITS 93 and (b) RITS 94. Several surface maps were combined to indicate the changing meteorological conditions encountered by the ship along the cruise track. The cruise tracks and location of impactor samples also are indicated. Measured sea level pressures along the cruise track are shown in the sidebar.

operated at sample and sheath airflow rates used by the manufacturer for the calibration. All flow rates were checked in the field and adjusted to better than 1% on a daily basis. The sheath air for both sizing systems was cleaned with absolute particle and charcoal filters. The APS diameters were converted to geometric diameter by dividing by the square root of a particle density of 1.9 g cm^{-3}, corresponding to that of sea salt. All DMA and APS results are plotted as the incremental distribution of number concentration, $\Delta N/\Delta \log D_p$, versus log of geometric particle diameter at 30% RH.

A seven-stage multijet cascade impactor [Berner et al., 1979] was used to collect samples for the determination of mass distributions of Cl$^-$, Br$^-$, NO$_3^-$, SO$_4^=$, methanesulfonate or MSA$^-$, Na$^+$, NH$_4^+$, K$^+$, Mg^{+2}, and Ca^{+2}. Samples were collected only when the concentration of particles greater than 15 nm in diameter indicated the sample air was free of contamination from the ship. In addition, samples were taken only when the wind speed was greater than 3 m s^{-1} and the wind direction was forward of the beam. The stages of the impactor had 50% aerodynamic cutoff diameters, D_{50}, of 0.125, 0.25, 0.5, 1.0, 2.0, 4.0, and 8.0 µm. For comparison to measurements of the number distribution the impactor aerodynamic diameters were converted to geometric diameters by dividing by the square root of an assumed density of 1.7 g cm^{-3}, which approximates that of ammoniated sulfate salts and sea salt at a relative humidity of 30%. The resulting 50% geometric cutoff diameters are 0.096,

0.19, 0.38, 0.77, 1.5, 3.1, and 6.1 µm. All impactor results are plotted as $\Delta m/\Delta \log D_p$ versus log of geometric particle diameter at 30% RH.

Tedlar films were used as the collection substrate for the six largest stages and a Millipore Fluoropore filter (1.0-µm pore size) was used for the smallest stage. The Millipore filter has a collection efficiency of 99% or greater for particles with diameters larger than 0.035 µm [Liu and Lee, 1976]. An impaction stage ($D_{50} \cong 10$ µm) at the inlet of the impactor was covered with silicone grease to prevent bouncing of large particles onto the downstream stages.

To avoid sample artifacts due to contaminated substrates, films were cleaned in an ultrasonic bath in 10% H$_2$O$_2$ for 30 min, rinsed 6 times in distilled, deionized water, and dried in an NH$_3$- and SO$_2$-free glove box. All handling of the substrates was done in the glove box. Blank levels were determined by loading the impactor with the substrates and deploying it at the sampling site for the length of a typical sampling period without pulling air through it. Following collection, the blanks were treated in an identical manner as the sample substrates. On average, the Na$^+$, NH$_4^+$, K$^+$, Mg^{+2}, Ca^{+2}, NO$_3^-$, and SO$_4^=$ blanks were 10, 30, 40, 8, 70, 5, and 8% of the sample values, respectively. The Cl$^-$, Br$^-$, and MSA$^-$ blanks were below detection limit.

The time period of impactor sampling ranged from 12 to 24 hours. After sample collection the material on the films and filter was extracted by first wetting with 1 mL of methanol and then
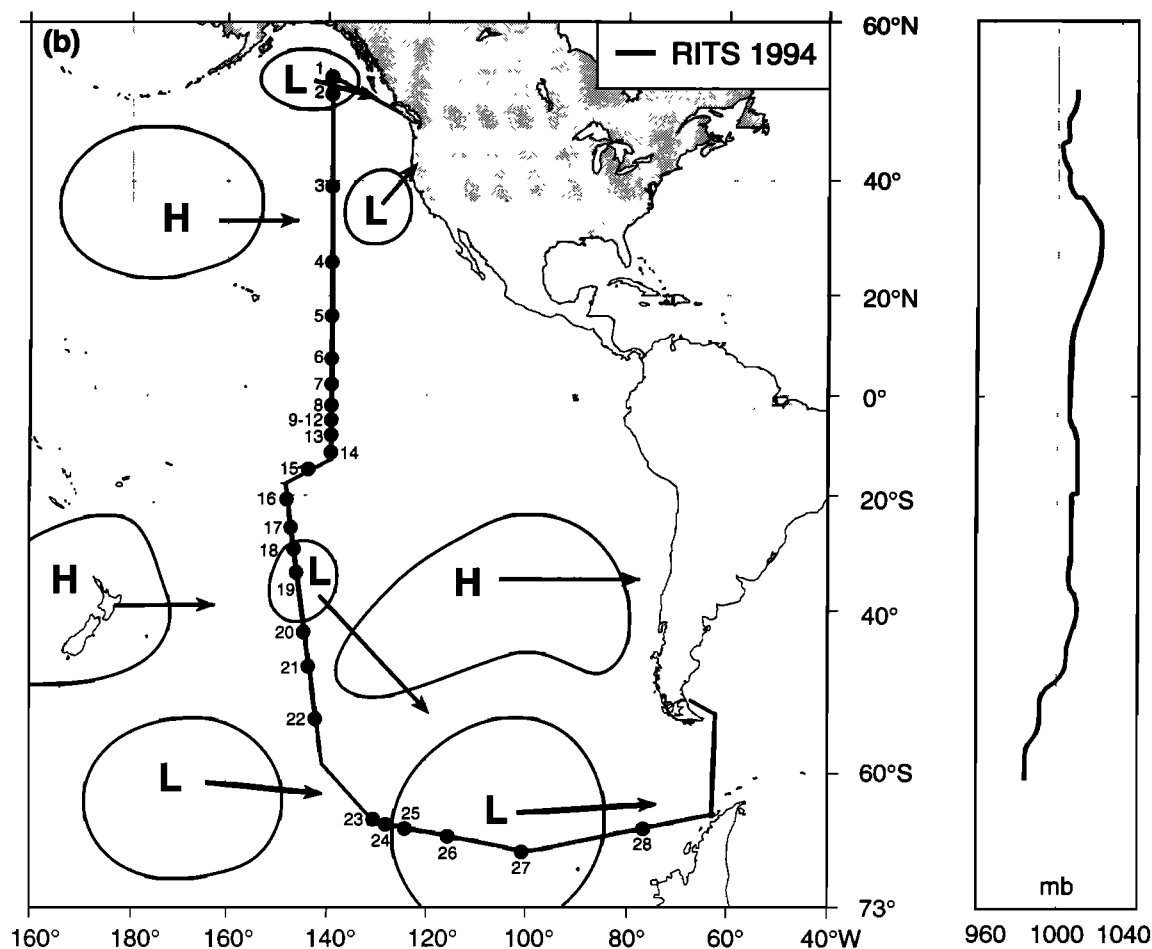
Figure 2. (continued)

adding 5 mL of distilled deionized water and sonicating for 15 min. Extracts were analyzed by ion chromatography. The cation analysis was done with a Dionex CS-12 column, 20-mM MSA eluant, and deionized water regenerant using the self-regenerating Dionex CSRS-1 suppressor system. Anion analysis was done with a Dionex AS-4A column, 0.76-mM NaHCO$_3$/2.0-mM Na$_2$CO$_3$ eluant, and 12.6-mM H$_2$SO$_4$ regenerant. MSA$^-$ analysis was performed with a Dionex AS-4 column, a 5-mM NaOH mobile phase to elute the weak organic acids followed by 100-mM NaOH to elute the stronger acids, and 12.6-mM H$_2$SO$_4$ regenerant. Non-sea-salt SO$_4^=$ concentrations were calculated from Na$^+$ concentrations and the molar ratio of sulfate to sodium in seawater of 0.0603 [*Holland*, 1978].

Measurements of the scattering coefficient, $\sigma_{sp,meas}$, were made at a wavelength of 0.55 μm with an integrating nephelometer [*Bodhaine et al.*, 1991] over a scattering angle, θ, where 8° ≤ θ ≤ 168°. Every 3 to 4 days the nephelometer was calibrated with the Rayleigh scattering value of CO$_2$ of 2.61 times air and was zeroed with particle-free air.

Ancillary measurements included surface temperature, dew point, wind speed, wind direction, and rawinsonde data. Rawinsonde balloons were launched at standard times of 0000 and 1200 GMT. Air mass back trajectories were calculated for up to 12 days using the hybrid single-particle Lagrangian integrated trajectories model, HY-SPLIT, based on wind fields generated by the medium-range forecast (MRF) model [*Draxler*, 1992]. Trajectories were terminated at the ship's location at 1000 mbar. Surface and upper air maps were obtained from the

National Weather Service archives to aid in the analysis of meteorological conditions and air motion.

2.2. Model Calculations

2.2.1. Calculation of scattering and backscattering by the total aerosol. The first step in calculating the light scattering (backscattering) due to each aerosol component was to test the ability of the Mie model to estimate accurately the scattering characteristics of the aerosol as a whole over all particle sizes and chemical components. To calculate the scattering due to the total aerosol, the Mie model was applied to the measured number distributions and the density and refractive index were derived from the measured chemical composition. These calculated scattering values then were compared to those measured directly with the nephelometer. The results of the comparison are discussed in section 3.4. Backscattering values also were calculated to derive the backscattered fraction b.

The model calculations described briefly here are presented in greater detail in *Marshall* [1994]. The scattering and backscattering efficiencies, Q_{sp} and Q_{bsp}, were obtained at discrete particle sizes by integrating over the scattered intensity function from 8° to 168° and 90° to 168°, respectively [*Bohren and Huffman*, 1983]. These efficiencies were then summed over the measured number distribution to yield the calculated scattering, $\sigma_{sp,calc}$, and backscattering, $\sigma_{bsp,calc}$, coefficients using

$$\sigma_{sp;bsp} = \sum Q_{sp;bsp}(D_i,\lambda,n) \pi \frac{D_i^2}{4} \frac{\Delta N}{\Delta \log D_i} \Delta \log D_i \quad (2)$$

where D_i is the geometric diameter of the measured particle size increment. Particles are assumed to be spherical, λ is the wavelength of incident light, and n is the particle refractive index. Even though the particles are subjected to decreasing RH as they pass through the heated sampling inlet, they are expected to remain spherical solution droplets due to hysteresis in the crystallization of the hygroscopic nss $SO_4^=$ and sea-salt aerosol components. Therefore the uncertainty associated with the assumption of spherical particles is expected to be small.

The number distributions used in (2) were obtained by averaging the measured DMA and APS data over the impactor sampling times. Particles were assumed to be homogeneous spheres distributed as an external mixture of two components: a nss $SO_4^=$ aerosol composed of nss $SO_4^=$, NH_4^+, and H_2O, and a sea-salt aerosol composed of Na^+, K^+, Mg^{+2}, Ca^{+2}, Cl^-, Br^-, NO_3^-, and sea-salt $SO_4^=$. The assumption of an external mixture is supported by the clear size separation of nss $SO_4^=$ and sea-salt aerosol into the submicron and supermicron size ranges (see section 3.2) and by individual particle analysis with an analytical electron microscope [McInnes et al., 1995a].

The particle number in any size increment was divided between the components based on the relative mass of the components determined from chemical analysis of the impactor stages. The water mass associated with the nss $SO_4^=$ aerosol component was assumed to be equivalent to that associated with an ammoniated sulfate salt at 30% RH neutralized to the degree indicated by the measured NH_4^+ to nss $SO_4^=$ molar ratio. This RH corresponds to the operating conditions of the nephelometer, sizing instrumentation, and impactor. Water was assumed to be a small fraction of the sea-salt component mass and was not included in the calculation. In cases where one or more of the sea-salt ion concentrations were unavailable, a concentration was calculated using the molar ratio of the ion to Na^+ in seawater [Holland, 1978].

The sea-salt mass was assigned a constant refractive index of $1.5-10^{-8}i$ [Kent et al., 1983] and a density of 1.9 g cm^{-3}. The density and refractive index of the nss sulfate component were determined by partitioning it into either a mixture of H_2SO_4 and NH_4HSO_4 or a mixture of NH_4HSO_4 and $(NH_4)_2SO_4$, according to the measured NH_4^+ to nss $SO_4^=$ molar ratio for each sample and impactor stage within that sample. The density of each mixture was derived from solution data for H_2SO_4 [Bray, 1970], NH_4HSO_4 [Tang and Munkelwitz, 1994], and $(NH_4)_2SO_4$ [Tang and Munkelwitz, 1991]; values ranged from 1.41 to 1.77 g cm^{-3}. The imaginary refractive index of the sulfate component was given a constant value of $10^{-7}i$ [Kent et al., 1983]. The real portion of the refractive index was estimated using the molar refraction method of Stelson [1990] and values of the electrolyte molar refraction from Tang and Munkelwitz [1994]; values ranged from 1.40 to 1.52.

The Mie calculations were performed at a wavelength of 0.55 μm corresponding to the central value of the nephelometer wavelength response. Sensitivity calculations using a gaussian wavelength response centered at 0.55 μm yielded scattering and backscattering coefficients within a few percent of the single wavelength calculations [Marshall, 1994].

There are uncertainties associated with the measurements which contributed to the uncertainty of $\sigma_{sp,calc}$ and $\sigma_{bsp,calc}$. The accuracy of the calculated scattering coefficients depends on the

completeness of the characterization of the chemical composition of the aerosol which in this case was determined by ion chromatography. To determine what portion of the aerosol mass was accounted for by the ion chromatography analysis, filters which collected the submicron fraction of the aerosol were analyzed gravimetrically and the resulting mass was compared to the mass from the ion chromatography (IC) analysis. Several precautions were taken to maintain the accuracy and precision of the gravimetric measurements. The balance was checked every tenth sample for instrumental drift with calibration weights. In addition, it was housed in a humidity- and temperature-controlled glove box located in a class 100 clean room. The resulting uncertainty was ±20%. Further details about the gravimetric analysis can be found in the work of McInnes et al. [1995b].

The average and standard deviation of the IC mass relative to the gravimetrically determined mass over all RITS 93 and RITS 94 samples was 80 ± 20%. It was difficult to correct for the missing mass in the scattering calculations, since it was not known which particle diameters within the submicron size range it was associated with. Therefore it was assumed that all of the scattering was due to the nss $SO_4^=$ and sea-salt components. In cases where the majority of the mass was nss $SO_4^=$ and sea salt, this assumption does not add any uncertainty to the scattering calculations. In cases where the IC mass is lower than the gravimetrically analyzed mass, the scattering due to nss $SO_4^=$ and sea salt will be overpredicted in proportion to the amount of missing mass. The largest error associated with this assumption would be a 20% overprediction of scattering by nss $SO_4^=$ or sea salt in a certain size range.

Other uncertainties include statistical fluctuation in the average number concentration and instrumental errors in particle sizing and counting due to drift of the airflow in the DMA and APS. An error propagation analysis was carried out to estimate the combined uncertainty of the calculated scattering. This analysis indicated an estimated uncertainty of about +20% and −13% in the calculation of both $\sigma_{sp,calc}$ and $\sigma_{bsp,calc}$ [Marshall, 1994].

2.2.2. Calculation of scattering and backscattering by the aerosol components. Calculations were performed to determine the fraction of the total scattering and backscattering due to the nss $SO_4^=$ and sea-salt aerosol components. The number concentration at each point in the measured number distribution was divided between the two components according to the measured ionic mass composition for the corresponding impactor interval. In this way the more detailed number distribution information was preserved. For example, the nss $SO_4^=$ aerosol number distribution was estimated from

$$\left(\frac{\Delta N}{\Delta \log D_p} \right)_{SO_4,aer} = \left(\frac{m_{SO_4,aer}/\rho_{SO_4,aer}}{m_{SO_4,aer}/\rho_{SO_4,aer} + m_{seasalt}/\rho_{seasalt}} \right) \frac{\Delta N}{\Delta \log D_p} \quad (3)$$

where $m_{SO_4,aer}$ and $m_{seasalt}$ are the nss $SO_4^=$ and sea-salt aerosol masses, $\rho_{SO_4,aer}$ and $\rho_{seasalt}$ are the nss $SO_4^=$ and sea-salt aerosol densities, and $\Delta N/\Delta \log D_p$ is the measured number distribution. The nss $SO_4^=$ aerosol light scattering and backscattering coefficients were calculated by substituting values of $(\Delta N/\Delta \log D_p)_{SO_4,aer}$ into (2). The sea-salt aerosol number

distribution and scattering (backscattering) coefficients were calculated similarly.

Equation (3) assumes that the chemically analyzed species account for the total measured number concentration and that the aerosol is an external mixture. A comparison of IC and gravimetrically analyzed mass indicate that the IC-identified aerosol components make up about 80% of the submicron aerosol mass [McInnes et al., 1995b]. Therefore in instances where other components are present, equation (3) will overestimate by up to 20% the number distribution as well as the scattering of the ionic aerosol components. No attempt was made to correct for this as it is not known how the unaccounted for mass is distributed with size. As stated above, the clear size separation of nss $SO_4^=$ and sea-salt aerosol into the submicron and supermicron size ranges (see section 3.2.) and results of individual particle analysis with an analytical electron micro-

scope [McInnes et al., 1995a] support the assumption of an externally mixed aerosol.

3. Results

3.1. Meteorology and Calculated Air Mass Back Trajectories

A composite of surface synoptic maps representing conditions during RITS 93 and RITS 94 are shown in Figures 2a and 2b, respectively, along with the cruise track and locations where impactor samples were collected. These figures are composites in the sense that they combine many surface weather maps to best approximate the synoptic features and motions encountered by the ship at each latitudinal region along the cruise track. Selected trajectories that are representative of both cruises are shown in Figure 3. Major synoptic features were similar for the two cruises.
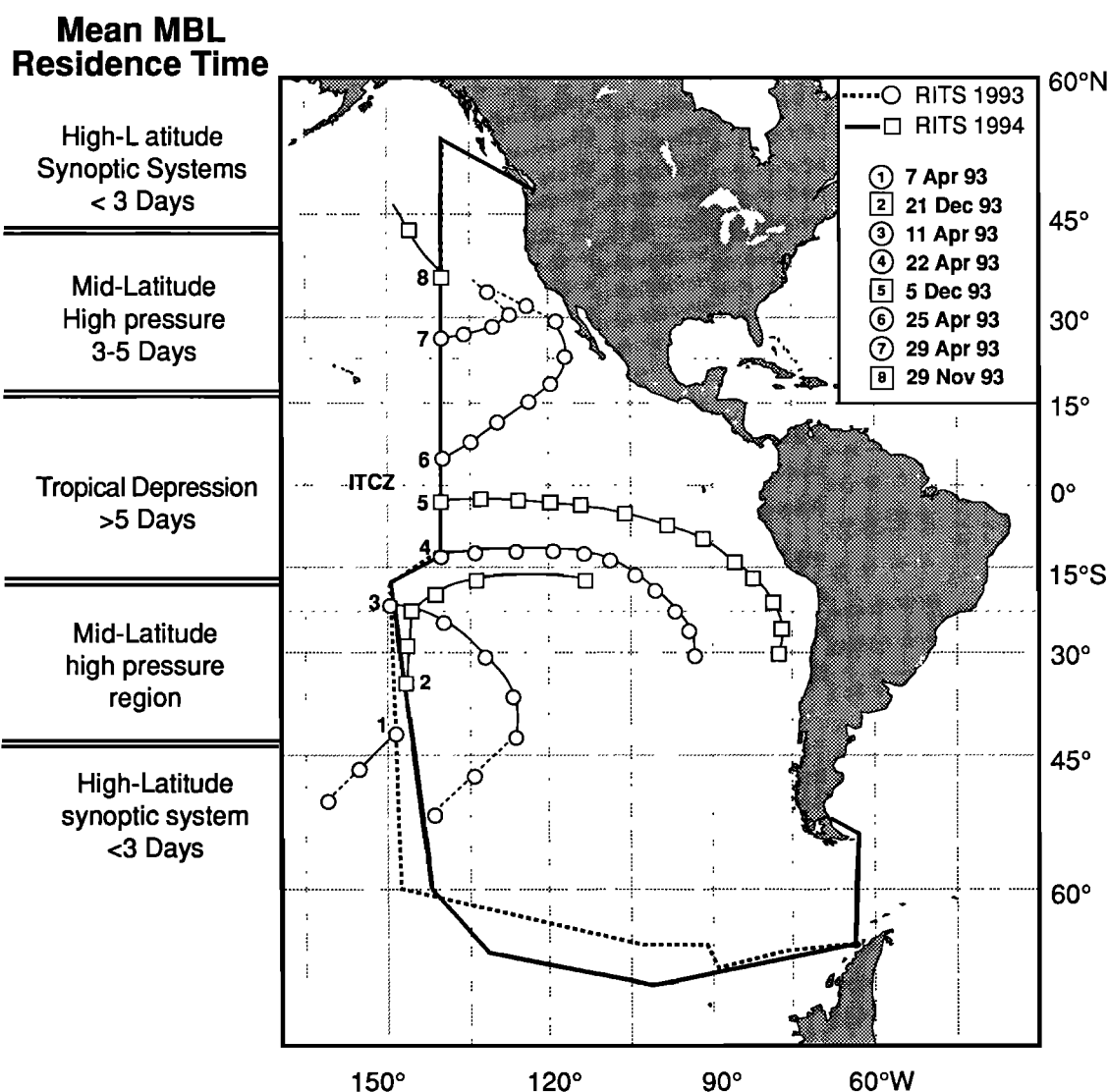

Figure 3. Back trajectories representative of those calculated for the RITS 93 and RITS 94 cruises. The trajectories end at the ship's position; each point represents 1 day back in time. The portion of each trajectory at less than 900-mbar pressure is plotted as a thick line, while the portion above that level is plotted as a dashed line. The 900-mbar surface was taken as the average height of the marine boundary layer based on analysis of the shipboard rawinsonde data. The sidebar indicates the marine boundary layer residence time which is defined as the length of time the air parcel and the aerosol it contained spent below 900 mbar prior to being sampled on the ship.

At high latitudes (>45° or 50°), in both the northern and the southern hemispheres, the passage of low-pressure systems from west to east occurred every few days. Sea level pressures in these regions were the lowest measured along both the RITS 93 and the RITS 94 cruise tracks. Subsidence of air from above the marine boundary layer height of about 1000 m was associated with frontal passages as indicated by trajectories (Figure 3, trajectory 1) and increases in the ultrafine and Aitken particle concentrations [Covert et al., 1995]. As a result, these regions had short marine boundary layer residence times of about 1 day. Here, the marine boundary layer residence time of an air parcel and the aerosol it contains is defined as the length of time the parcel spent below 900 mbar prior to being sampled on the ship. This residence time was estimated from the calculated back trajectories.

Belts of strong high-pressure systems moving from west to east existed in the midlatitudes from about 40°S to 20°S and from 20°N to 40°N. The latitudes given are approximate as the position of these systems varied with season and year. The location of the ship relative to the high-pressure systems determined the trajectories of the air being sampled. During RITS 93, as the ship traveled north from 50°S to 20°S, it remained within one well-developed high. The transit of the ship from the low-pressure region of the higher latitudes to this high-pressure region in the midlatitudes is evidenced by the sharp increase in sea level pressure from 960 to 1030 mbar (Figure 2a). On the equatorward side of the high, calculated trajectories were from the southeast (Figure 3, trajectory 3). This air was transported from the free troposphere at 55°S through the southeast sector of the high. Subsidence followed by transport along the edge of the high resulted in boundary layer residence times of about 4 days. On the poleward side of the high, air subsided from the free troposphere and was transported along the southern edge of the high. Here, boundary layer residence times were about 3 days.

During RITS 94, while traveling from north to south, the ship entered the southern hemisphere midlatitudes as a low-pressure system near Tahiti formed between two highs. The ship moved with the low-pressure system from about 20°S to 40°S. Hence there is only a gradual decrease in the measured sea level pressure as the ship moved from 45°S to 60°S. Trajectories (Figure 3, trajectory 2) indicate that the sampled air was transported from the northeast along the surface to this low-pressure region. The sampled air had a boundary layer residence time of up to 5 days.

In the northern hemisphere midlatitudes during RITS 93 the ship traveled through a pseudostationary high from about 20°N to 40°N. On the equatorward side of the high the sampled air was transported along the edge of the high from the northeast with a boundary layer residence time of 3 to 5 days (Figure 3, trajectory 7). High number and sulfate mass concentrations indicate that this air had been continentally influenced prior to its arrival at the ship. During RITS 94, as the ship moved from north to south, a low-pressure system was encountered at 55°N and again near 45°N. The ship traveled with the second low until about 20°N. Trajectories (Figure 3, trajectory 8) were of a more marine origin than for RITS 93, with sampled air having been transported from the northwest with a boundary layer residence time of at least 2 days.

The well-developed midlatitude highs in both the northern and the southern hemispheres led to a tropical depression between about 20°S and 20°N. This low-pressure belt is indicated by the decrease in measured sea level pressure for both

RITS 93 and RITS 94. Within this belt, air flowing around the high-pressure systems resulted in relatively stable and consistent marine boundary layer trade wind flow for both cruises. Easterly trajectories (Figure 3, trajectories 4, 5, 6) indicated that the sampled air masses had boundary layer residence times of up to or more than 7 days. Based on atmospheric CO concentrations, the Intertropical Convergence Zone (ITCZ) was located at about 2°N during RITS 93 and between 5° and 10°N during RITS 94 [Bates et al., 1995].

3.2. Size Distributions

Number- and chemical mass-size distributions were analyzed for the regions described above as they each give information about the aerosol. Modal features of the number distribution reveal information about the age of the aerosol or degree to which the aerosol has been affected by coagulation, condensation, and cloud processes [Covert et al., 1995]. Chemical mass distributions yield information about the aerosol source. Plots of average number distributions for different latitudinal regions and the variability observed over these regions are shown in Figures 4 (RITS 93) and 5 (RITS 94). The measured number distribution data extend to a diameter of 10 μm. They are only shown to 0.6 μm, however, as larger diameters are indistinguishable from the x axis on the scale used for the y axis. Examples of data for the entire size range are shown as volume-size distributions in Figure 6. Particle number, nss $SO_4^=$, and Na^+ size distributions are presented as contour plots of concentration versus size and sample number (or latitude) in Figures 7 through 9. These contour plots allow for a more detailed presentation of the data as a time series than would be possible with a sequence of two-dimensional plots.

The Aitken mode dominated the number distribution in the high latitudes (>45°S and >45°N) during both RITS 93 (Figures 4a, 4f, and 7a) and RITS 94 (Figures 5a, 5f, and 7b). Figures 4a, 4f, 5a, and 5f also indicate the high variability in the Aitken mode number concentration in these regions. This type of distribution is indicative of intrusion of air from the upper troposphere into the boundary layer [Clarke, 1993; Covert et al., 1995]. Aerosol growth from the Aitken to the accumulation mode size range due to vapor condensation and cloud processing is thought to occur mainly in the boundary layer and in stratus and stratocumulus clouds [Hegg et al., 1992; Quinn et al., 1993; Hoppel et al., 1994]. The short boundary layer residence times associated with these distributions prevented the increase of number and nss $SO_4^=$ mass in the accumulation mode (Figures 8a and 8b).

The difference in the position of the ship relative to the midlatitude highs in the southern hemisphere for RITS 93 and RITS 94 is reflected in a difference in the measured number distributions (Figures 4b and 5b). During RITS 93 the ship moved through one high-pressure system between 42°S and 20°S. The free tropospheric source of the sampled air is indicated by the Aitken modal diameter, which is less than 20 nm [Covert et al., 1995], and dominance of the Aitken mode (Figures 4b and 7a). Further north, from 20°S to 18°S, the sampled air had spent slightly more time in the boundary layer, so that the Aitken modal diameter was larger than 20 nm (Figure 4c). The relatively short boundary layer residence time led to low accumulation mode nss $SO_4^=$ mass concentrations (Figure 8a).

During RITS 94 the ship was moving with a low-pressure system within this same region. From both 42°S to 20°S (Figure
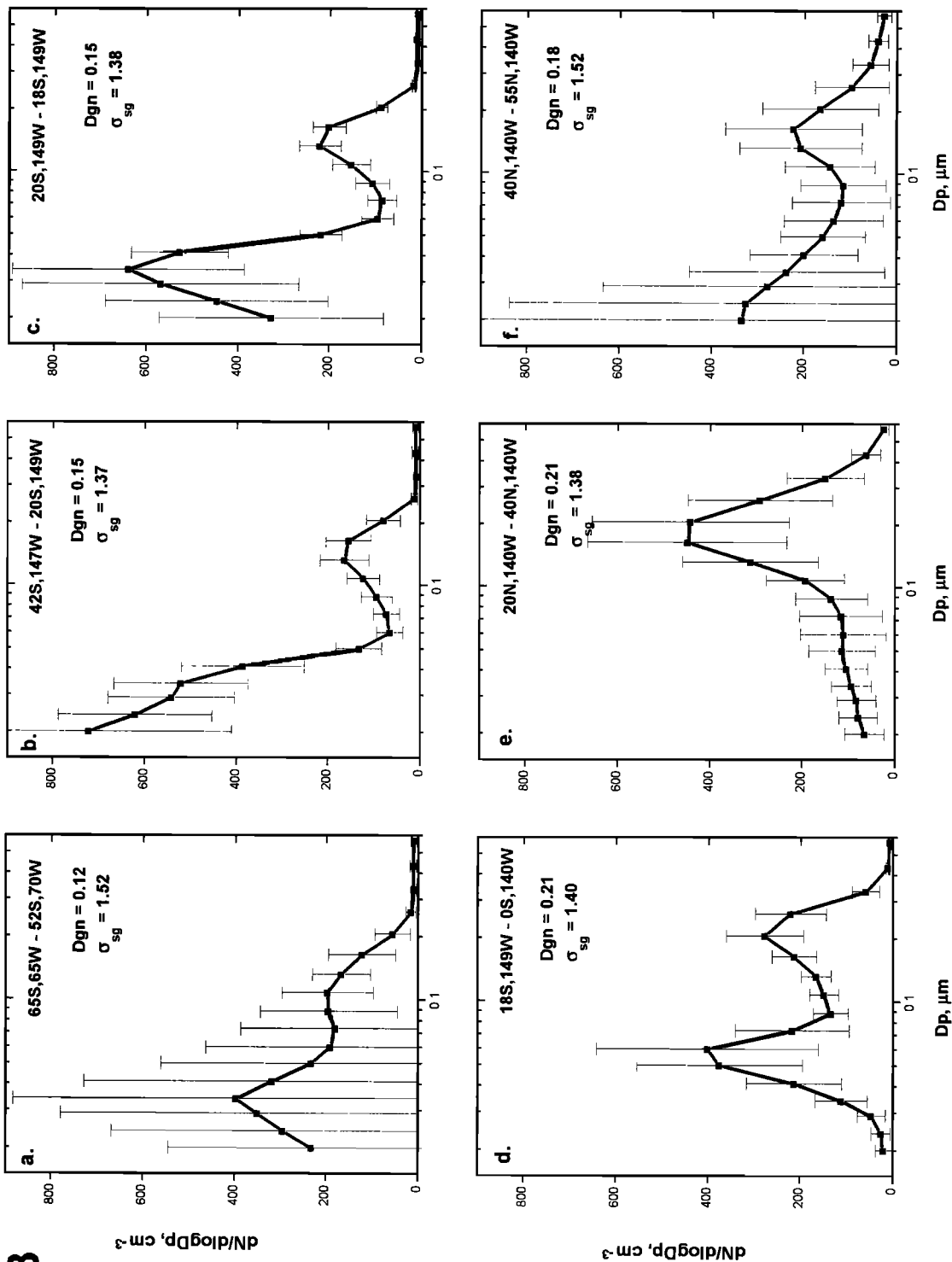
Figure 4. Average and standard deviation of the number-size distribution for latitudinal regions during RITS 93. The distributions are averages over all measurements taken every 10 min between (a) 65°S and 52°S, (b) 42°S and 20°S, (c) 20°S and 18°S, (d) 18°S and 0°, (e) 20°N and 40°N, and (f) 40°N and 55°N. The standard deviation represents the variability of the size distribution for the latitudinal region. DISTFIT (version 1.10, TSI) was used to calculate the modal parameters. The number-size distribution was measured to 10 μm, but values above 0.6 μm were indistinguishable from the x axis on the y axis scale shown here.
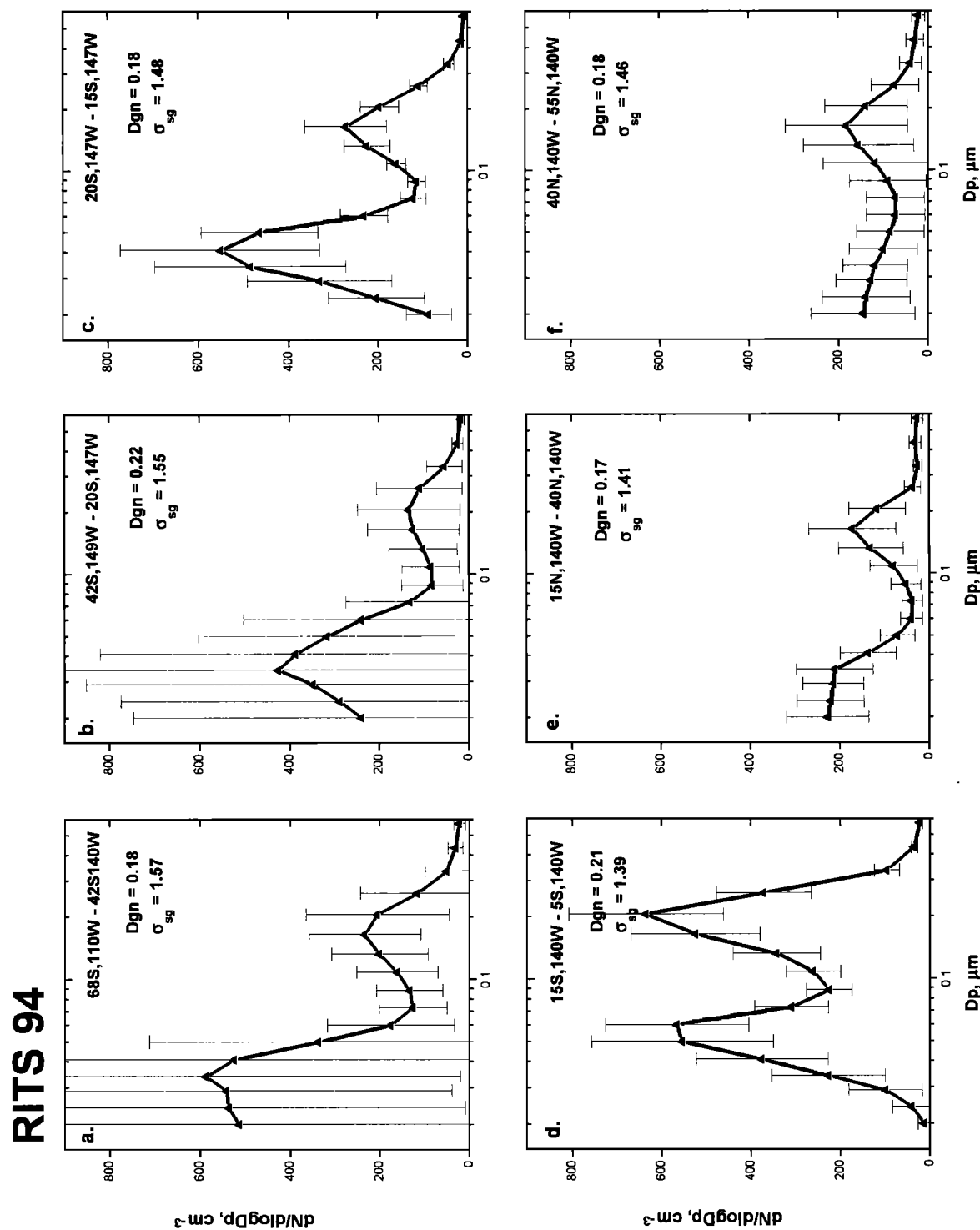
Figure 5. Average of the number-size distribution for latitudinal regions during RITS 94 between (a) 68°S and 42°S, (b) 42°S and 20°S, (c) 20°S and 15°S, (d) 15°S and 5°S, (e) 15°N and 40°N, and (f) 40°N and 55°N.
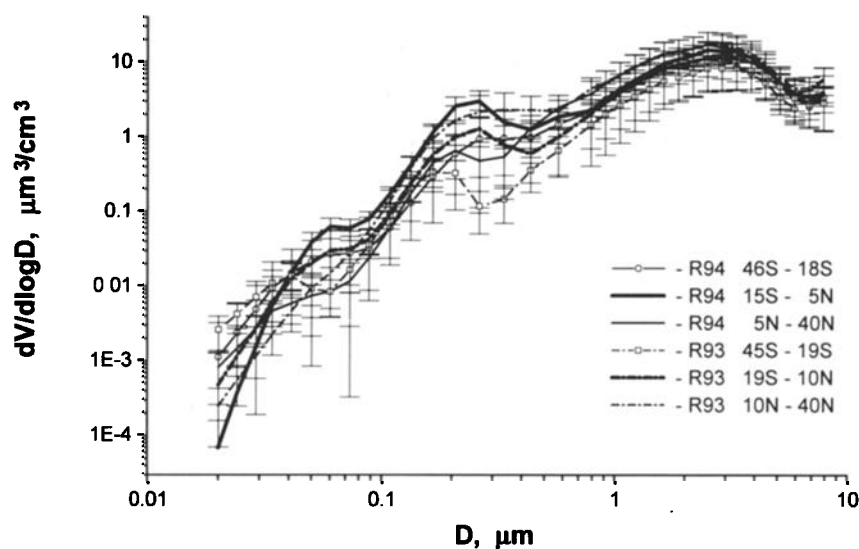
Figure 6. Average and standard deviation of the volume-size distribution for latitudinal regions during RITS 93 and RITS 94. Volume-size distributions were calculated from the measured number-size distributions.
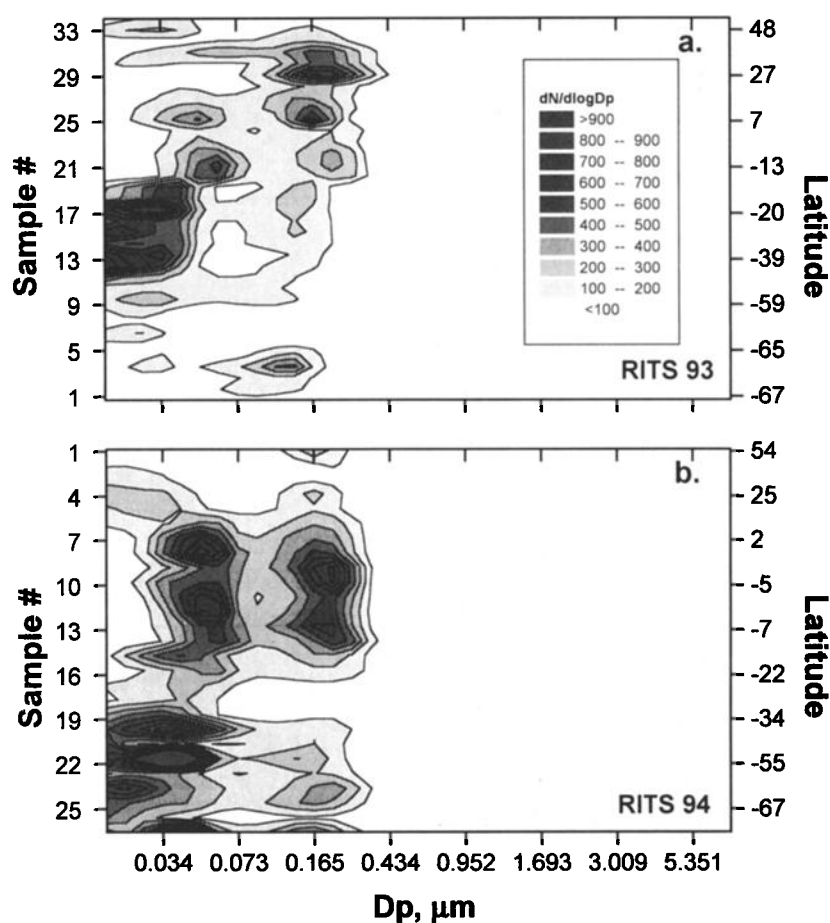

Figure 7. Contour plots of the number-size distribution ($\Delta N/\Delta \log D_p$) as a function of sample number and latitude for (a) RITS 93 and (b) RITS 94. The size distributions are plotted as averages over the time periods of the impactor samples.
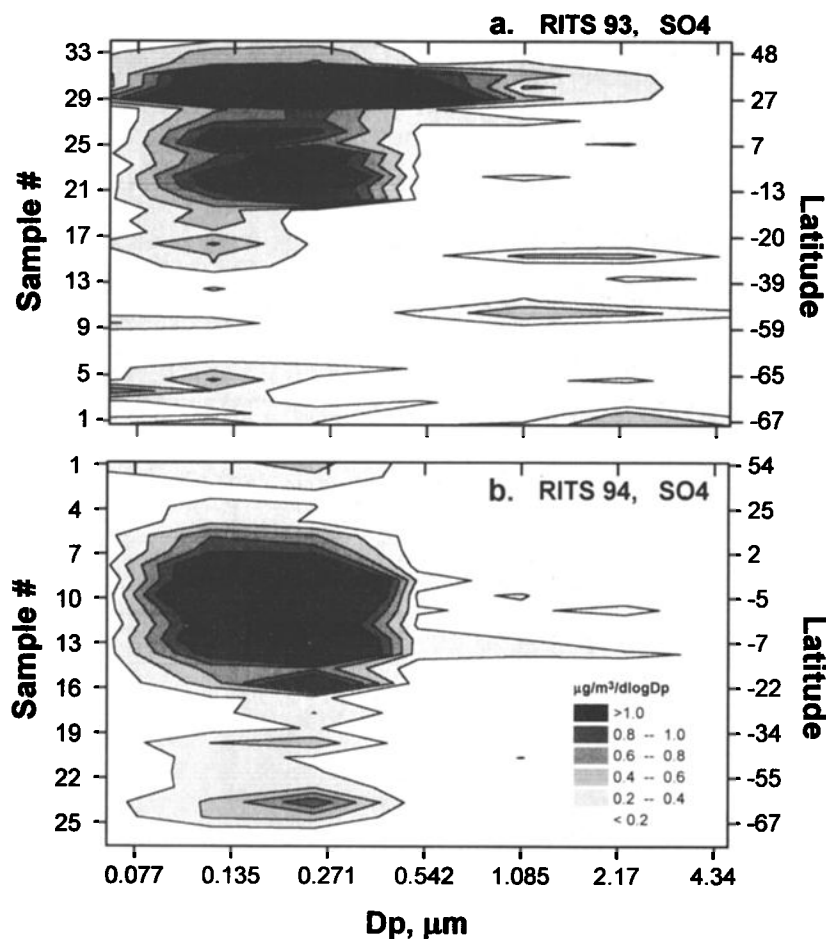
Figure 8. Contour plots of the nss $SO_4^=$ mass-size distribution ($\Delta m/\Delta log D_p$) as a function of sample number and latitude for (a) RITS 93 and (b) RITS 94.

5b) and 20°S to 18°S (Figure 5c) the Aitken modal diameter was between 20 and 30 nm, indicating the sampled air did not have a recent free tropospheric source. Non-sea-salt $SO_4^=$ concentrations were low (Figure 8b), suggesting that wet removal of aerosol associated with the low-pressure system had occurred.

The stable marine boundary layer in the tropical depression between the midlatitude highs (20°S to 20°N) led to long boundary layer residence times during both cruises. As a result the aerosol was well aged, as indicated by bimodal number distributions and relatively high number concentration in the accumulation mode for both RITS 93 (Figures 4d and 7a) and RITS 94 (Figures 5d and 7b). Here, age is not strictly a time but refers to time dependent boundary layer processing of the aerosol which results in characteristic changes in the number distribution. The longer boundary layer residence times allowed for the deposition of vapors onto particles and the passage of particles through clouds leading to particle growth, as indicated by high nss $SO_4^=$ concentrations (Figures 8a and 8b) in the accumulation mode.

Number distributions measured during RITS 93 in the northern hemisphere midlatitudes (20°N to 40°N) were dominated by the accumulation mode (Figures 4e and 7a). Similarly, nss $SO_4^=$ mass distributions (Figure 8a) were dominated by a very large and broad accumulation mode. These size distributions, coupled with the trajectories from the northeast, indicate that the sampled air had been influenced by continental sources

before reaching the ship. The RITS 94 number (Figures 5e and 6b) and nss $SO_4^=$ (Figure 8b) size distributions measured in this same region were lower in concentration and not so dominated by the accumulation mode. This is consistent with the more marine trajectories from the northwest.

Accumulation mode geometric number mean diameters, D_{gn}, and standard deviations, σ_{sg}, were calculated for the average size distributions shown in Figures 4 and 5 using DISTFIT (version 1.10, TSI). Highest D_{gn} values of 0.21 to 0.22 µm occurred in the tropics where boundary layer residence times were up to 7 days (RITS 93, Figure 4d and RITS 94, Figure 5d), the mid-latitudes of the northern hemisphere for air that had been advected from North America (RITS 93, Figure 4e), and the midlatitudes of the southern hemisphere for air that had been transported along the surface for several days prior to being sampled (RITS 94, Figure 5b). Lower values of 0.12 to 0.18 µm were associated with aerosol in air masses that had subsided from the free troposphere and spent 3 or less days in the boundary layer. Values of σ_{sg} ranged from 1.37 to 1.57. Particular values did not appear to correlate to specific meteorological conditions.

For all regions of RITS 93, high coarse mode ($D_p > 0.5$ µm) Na^+ mass concentrations corresponded to regions of higher wind speeds, indicating the wind-driven production and transport of sea-salt aerosols (Figure 9a). A similar but less strongly correlated pattern was observed for RITS 94 (Figure 9b). The relationship between local wind speed and sea-salt aerosol mass
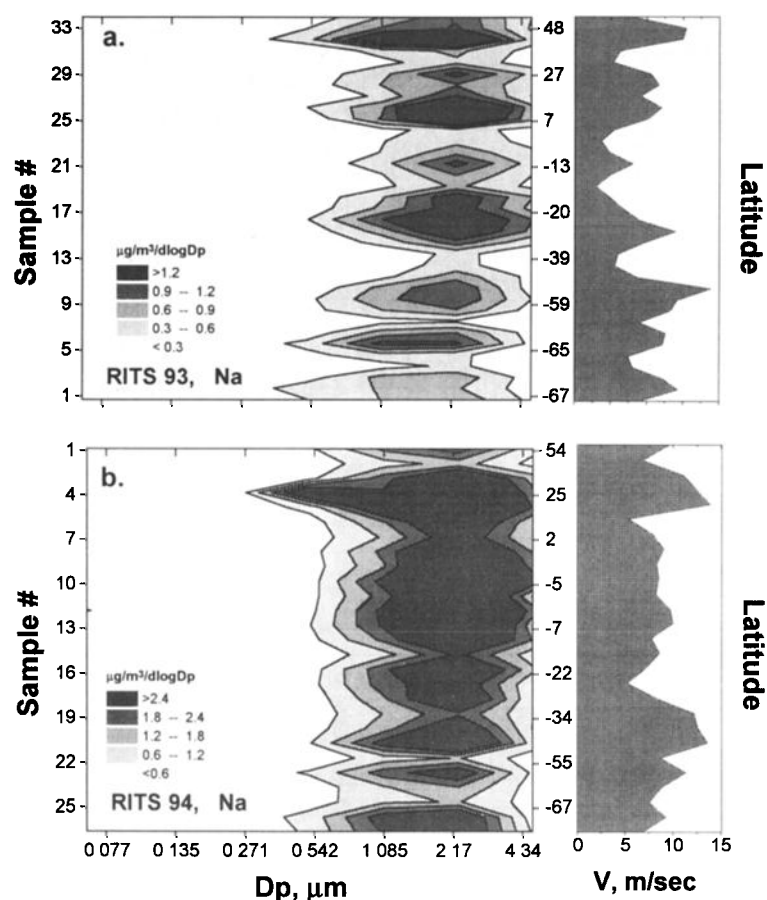
Figure 9. Contour plots of the Na^+ mass-size distribution $(\Delta m/\Delta logD_p)$ as a function of sample number and latitude for (a) RITS 93 and (b) RITS 94. The latitudinal distribution of wind speed in meters per second also is shown.

concentration varied by a factor of 2, depending on the speed and direction of the wind relative to the ship. Loss of larger particles at the inlet and in the sample lines will dampen the measured effect of wind speed on sea-salt mass. The relationship also is affected by the long-range transport of sea-salt aerosol in addition to locally produced sea salt. For these reasons a quantification of the relationship between wind speed and sea-salt mass is inappropriate for this study.

Five of the seven instances of measurable nss $SO_4^=$ mass in the coarse mode during RITS 93 (Figure 8a) corresponded to regions of high wind speeds and coarse mode Na^+ concentrations. It is possible that the enhanced coarse mode surface area led to an increased deposition of SO_2 onto the sea-salt aerosol. A knowledge of the SO_2 concentration, the rate of SO_2 transport to the sea-salt particles, the rate of SO_2 deposition onto the sea-salt aerosol, and the sea-salt deposition rate to the surface is needed to confirm this, however.

A comparison of Figures 8 and 9 shows the clear separation of the nss $SO_4^=$ and sea-salt modes at a geometric diameter of about 0.5 μm (0.7-μm aerodynamic diameter) at the sampling humidity of 30% RH. This same separation diameter was found for aerosol sampled in the tropical Pacific during the Marine Aerosol and Gas Exchange (MAGE) experiment in 1992 [*Quinn et al.*, 1995] and therefore appears to be a common feature of marine boundary layer aerosol.

3.3. Mass Fraction of nss $SO_4^=$, Sea Salt and MSA⁻ Aerosol Components

The mass fraction of an aerosol component is defined as its mass divided by the total mass of the aerosol. Because of the different detection limits of the gravimetric and IC analyses, sampling times were different for the two sets of samples. To avoid having to average the results of several IC samples over the time period of one corresponding gravimetric sample, mass fractions are given in terms of the mass of the aerosol component relative to the total ionic mass.

The aerosol was divided into a nss $SO_4^=$ aerosol component composed of nss $SO_4^=$ and NH_4^+, a sea-salt aerosol component composed of Na^+, K^+, Mg^{+2}, Ca^{+2}, Cl^-, Br^-, NO_3^-, and sea-salt $SO_4^=$ and a MSA⁻ component. The mass fraction of the submicron and supermicron portion of each of these components was calculated by summing over the appropriate impactor stages. The results are shown in Table 1. Mass fractions of the nss $SO_4^=$ and sea-salt aerosol components are shown as a function of sample number and latitude in Figures 10a and 10b for RITS 93 and RITS 94, respectively. The residual ionic mass not accounted for in the figures is MSA⁻.

For RITS 93, three regions of higher nss $SO_4^=$ aerosol mass fractions are apparent. These regions had the longest boundary layer residence times and/or the largest potential source of

Table 1. Percent Mass Fractions of Ionic Aerosol Components Relative to Measured Total or Submicron Ionic Mass

Component[a]	RITS 93			RITS 94		
	Average	Standard Deviation	Range	Average	Standard Deviation	Range
Percent Mass Fraction of Total Measured Ionic Mass						
Super-μm sea salt	81	9	58–93	82	5.8	69–92
Sub-μm sea salt	10	7	1.4–28	8.3	4.6	2.7–19
Sub-μm nss $SO_4^=$	7	8.3	0.2–34	6	3.7	0.9–13
Super-μm nss $SO_4^=$	1.3	1	0.2–3.8	0.8	1	0.1–5.5
Sub-μm MSA⁻	0.39	0.48	0.08–2.7	1.0	1.6	0.03–6.0
Super-μm MSA⁻	0.24	0.37	0.03–2.0	0.40	0.29	0.03–1.1
Percent Mass Fraction of Submicron Measured Ionic Mass						
Sub-μm sea salt	55	79	10–98	54	22	21–91
Sub-μm nss $SO_4^=$	36	28	2–90	39	23	6–76
Sub-μm MSA⁻	2.1	1.7	0.31–10	5.5	6.6	0.37–24

Percent mass fractions are defined as the mass of the aerosol component divided by the measured ionic mass.

[a] The nss $SO_4^=$ aerosol component includes the associated NH_4^+ mass. The sea-salt aerosol component includes Na^+, K^+, Mg^{+2}, Ca^{+2}, Cl^-, Br^-, NO_3^-, and sea-salt $SO_4^=$.

sulfate aerosol. From 27°N to 38°N where, according to number and nss $SO_4^=$ concentrations, continentally influenced aerosol had been advected in a nonprecipitating air mass from North America, the mass fraction of nss $SO_4^=$ aerosol was the highest measured, ranging from 23 to 37%. In the tropics, between 19°S and 2°N, where boundary layer residence times were the longest

Figure 10. Mass fractions of the submicron nss $SO_4^=$, supermicron nss $SO_4^=$, submicron sea-salt, and supermicron sea-salt aerosol components as a function of sample number and latitude for (a) RITS 93 and (b) RITS 94. Mass fractions are defined as the mass of the aerosol component divided by the total ionic mass as measured by ion chromatography. Residual ionic mass not accounted for by these aerosol components is MSA⁻.

encountered (up to 7 days) and atmospheric DMS concentrations were about 100 parts per trillion by volume (pptv), the mass fraction was 5 to 20%. Values up to 10% occurred between 65°S and 67°S where atmospheric DMS concentrations of 200 pptv were among the highest measured along the cruise track. Elsewhere, marine boundary layer residence times were less than 5 days and DMS concentrations were less than 100 pptv.

A similar pattern is seen for RITS 94. Mass fractions of nss $SO_4^=$ aerosol of 10% were observed between 65°S and 67°S. This cruise reached the high southern latitudes during the austral summer when ocean productivity in this region is at its maximum. The atmospheric DMS concentrations of up to 650 pptv were the highest measured during both cruises. The higher mass fractions in the tropics also were repeated during RITS 94 where the values ranged from 8 to 16%. Mass fractions were not enhanced between 20°N and 40°N during RITS 94, however, as the sampled air had a northwest trajectory and had spent several days over the ocean before reaching the ship.
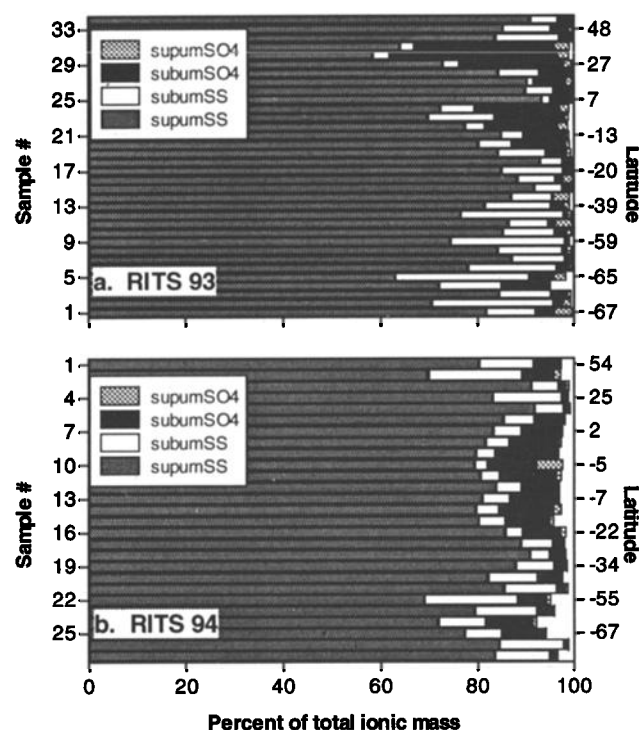
3.4. Comparison of Measured and Calculated Light Scattering

For RITS 94, $\sigma_{sp,meas}$ ranged from 7.8 to 40 × 10^{-6} m⁻¹ with an average and standard deviation of 18 ± 6.8 × 10^{-6} m⁻¹ (Figure 11a). Values of $\sigma_{sp,calc}$ were similar, ranging from 4.3 to 37 × 10^{-6} m⁻¹ with an average and standard deviation of 16 ± 6.7 × 10^{-6} m⁻¹. A regression of the measured versus the calculated values yields an r^2 value of 0.9 (Figure 11b). This agreement is within the uncertainty of the measurement and modeling methods and indicates that the Mie model is able to parameterize accurately the chemical and scattering characteristics of the total aerosol. The $\sigma_{bsp,calc}$ values ranged from 0.41 to 3.4 × 10^{-6} m⁻¹ with an average and standard deviation of 1.5 ± 0.62 × 10^{-6} m⁻¹. The backscattered fraction based on $\sigma_{sp,calc}$ and $\sigma_{bsp,calc}$ ranged from 0.088 to 0.102 and averaged 0.095 ± 0.004.

For RITS 93, $\sigma_{sp,meas}$ values were incorrect as a result of drift in the sample and dilution airflows within the nephelometer. Based on the agreement between the measured and calculated values for the RITS 94 data set, $\sigma_{sp,calc}$ instead of $\sigma_{sp,meas}$ values were used in all further RITS 93 data analyses. RITS 93 values
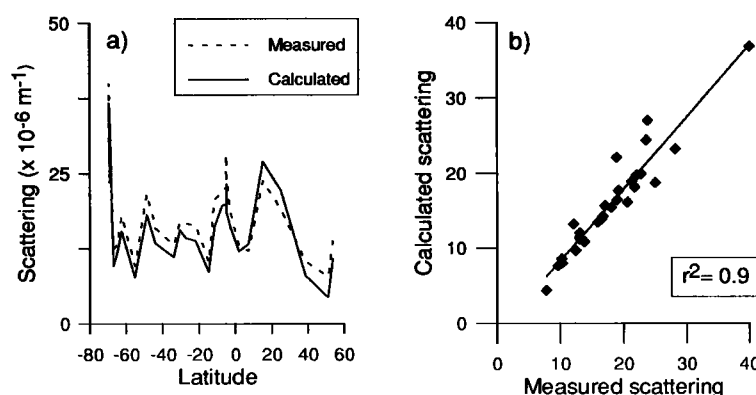
Figure 11. (a) Latitudinal distribution of $\sigma_{sp,meas}$ and $\sigma_{sp,calc}$ averaged over the time period of the impactor samples for RITS 94 and (b) regression of $\sigma_{sp,meas}$ versus $\sigma_{sp,calc}$ for RITS 94.

of $\sigma_{sp,calc}$ ranged from 6.4 to 36 × 10^{-6} m^{-1} with an average and standard deviation of 16 ± 9.3 × 10^{-6} m^{-1}. The $\sigma_{bsp,calc}$ values ranged from 0.53 to 3.7 × 10^{-6} m^{-1} with an average and standard deviation of 1.5 ± 0.87 × 10^{-6} m^{-1}. The backscattered fraction, then, ranged from 0.089 to 0.102 and averaged 0.095 ± 0.003.

3.5. Light Scattering and Backscattering Calculated for nss $SO_4^=$ and Sea-Salt Aerosol

Calculation of the light scattering and backscattering due to nss $SO_4^=$ and sea-salt aerosol was described in detail in section 2.2.2. The aerosol was modeled as two externally mixed components; these were 1) nss $SO_4^=$ with associated NH_4^+ and H_2O mass and 2) sea salt. Mie theory was applied to each component's size distribution to determine its absolute and fractional contribution to scattering and backscattering by the total aerosol.

The extent to which an aerosol component contributes to the scattering and backscattering by the aerosol as a whole depends on the size distribution of the component relative to that of the total aerosol. This is well illustrated by comparing the latitudinal distributions of the calculated fractional nss $SO_4^=$ light scattering for RITS 93 and RITS 94 in Figures 12a and 12b to the corresponding nss $SO_4^=$ mass fractions (Figures 10a and 10b) and mass distributions (Figures 8a and 8b). The latitudinal pattern of the nss $SO_4^=$ mass fractions is repeated but amplified in the nss $SO_4^=$ light scattering. This amplification is a result of the dependence of scattering on particle size and the concentration of the nss $SO_4^=$ mass within the accumulation mode where it has the highest specific scattering per unit volume (see Figure 1).

For RITS 93 the scattering calculated for the nss $SO_4^=$ aerosol component was highest between 27°N and 38°N (58 to 65%), in the tropics (13 to 50%), and around 65°S (11 to 16%). The nss $SO_4^=$ backscattering was highest in these same regions. From 27°N to 38°N it made up 52 to 60% of the total backscattering, in the tropics from 11 to 45%, and near 65°S from 8 to 12%. The absolute values of the nss $SO_4^=$ scattering and backscattering coefficients for these regions are listed in Table 2.

For RITS 94 the nss $SO_4^=$ scattering also followed the latitudinal distribution of the nss $SO_4^=$ mass fractions and size distributions. Highest values occurred near 65°S (38%) and in the tropics (26 to 48%). Non-sea-salt $SO_4^=$ backscattering values also were highest in these regions, being about 35% of the backscattering by the total aerosol at 65°S and 17 to 46% of the total in the tropics. Unlike RITS 93 the low nss $SO_4^=$ mass fractions between 20°N and 40°N and lower concentrations of

nss $SO_4^=$ in the accumulation mode resulted in low nss $SO_4^=$ scattering values for this region.

For both RITS 93 and RITS 94 the average mass fractions of submicron nss $SO_4^=$ and submicron sea-salt aerosol had similar values (Table 1). The average values of nss $SO_4^=$ and submicron sea-salt scattering also were similar (Table 2). Therefore for cases where the mass concentrations of submicron nss $SO_4^=$ and sea salt are comparable, scattering by sea salt within the submicron size range cannot be neglected. For both cruises, 80% of the total ionic mass was supermicron sea-salt aerosol. Yet, it made up only 42 to 48% of the scattering by the total aerosol as it occurred outside of the most efficient size range for scattering by particles.
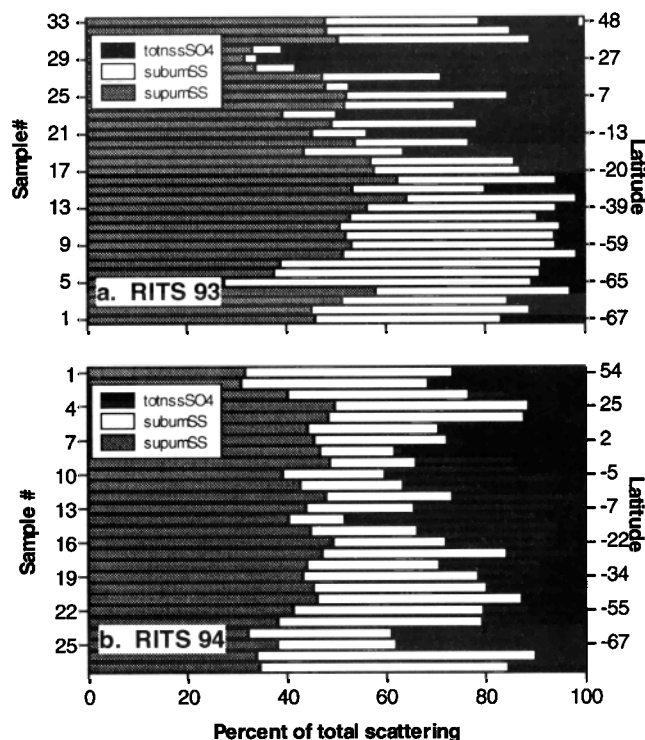

Figure 12. Calculated light scattering for the nss $SO_4^=$, submicron sea-salt, and supermicron sea-salt aerosol components as a function of sample number and latitude for (a) RITS 93 and (b) RITS 94. Values are presented as percent of the total scattering due to each component where the total scattering is a sum of the calculated scattering for these three components.

Table 2. Scattering and Backscattering Coefficients Calculated for nss $SO_4^=$, Submicron Sea Salt, and Supermicron Sea-Salt Aerosol Components for Latitudinal Regions Where nss $SO_4^=$ Had the Largest Contribution to Scattering by Total Aerosol

Coefficient, $\times 10^{-6}$ m^{-1}	NH Midlatitudes 27°N to 38°N		Tropics 20°S to 20°N		SH High Latitudes 65°S to 67°S	
	RITS 93	RITS 94	RITS 93	RITS 94	RITS 93	RITS 94
$\sigma_{sp,SO_4,aer}$	11–18	1.8–2.4	1.4–9.4	2.9–9.3	1.3–2.1	1.7–5.6
$\sigma_{sp,sub,seasalt}$	0.43–2.5	2.9–8.6	0.72–11	1.8–11	2.5–13	2.3–18
$\sigma_{sp,sup,seasalt}$	5.2–10	3.2–11	2.6–19	3.8–13	2.3–6.7	3.7–13
$\sigma_{bsp,SO_4,aer}$	0.89–1.4	0.12–0.16	0.12–0.62	0.22–0.83	0.1–0.13	0.33–0.39
$\sigma_{bsp,sub,seasalt}$	0.1–0.23	0.23–0.71	0.10–0.95	0.16–0.85	0.21–1.0	0.19–1.5
$\sigma_{bsp,sup,seasalt}$	0.57–1.1	0.35–1.2	0.28–2.1	0.41–1.5	0.27–1.1	0.41–1.5

NH, northern hemisphere; SH, southern hemisphere.

3.6. Mass Scattering Efficiencies for the nss SO_4^- and Sea-Salt Aerosol Components

Mass scattering efficiencies for individual aerosol components can be estimated from a multiple linear regression of the mass concentration of each aerosol component against the scattering coefficient for the whole aerosol. For the RITS 93 and RITS 94 data sets a regression of the following form, including only the major aerosol components, was used to obtain weighted averages of the scattering efficiencies

$$\sigma_{sp,calc} = \alpha_{sp,SO_4,ion}m_{SO_4,ion} + \alpha_{sp,sub,seasalt}m_{sub,seasalt} + \alpha_{sp,sup,seasalt}m_{sup,seasalt}$$ (4)

The mass scattering efficiency of nss $SO_4^=$ ($\alpha_{sp,SO_4,ion}$) is given in terms of the unit mass of nss $SO_4^=$ ion as it is the ion concentration or column burden that is predicted by chemical transport models [e.g., *Langner and Rodhe*, 1991]. Values of $m_{SO_4,ion}$ include both the submicron and supermicron size fractions since the majority of the nss $SO_4^=$ mass (>75%) occurred in the submicron size range and this is the size range expected to have the most significant effect on scattering by the total aerosol.

Unlike the nss $SO_4^=$ aerosol component, the majority of the sea-salt aerosol mass was in the supermicron size fraction which will not have a large influence on scattering by the total aerosol unless it overwhelms the total particle mass concentration. To consider the more relevant submicron fraction, the sea-salt component was divided into submicron and supermicron size ranges resulting in a submicron mass scattering efficiency ($\alpha_{sp,sub,seasalt}$) and a supermicron mass scattering efficiency ($\alpha_{sp,sup,seasalt}$). Mass backscattering efficiencies for the aerosol components were calculated by substituting the calculated backscattering coefficient, $\sigma_{bsp,calc}$, for the whole aerosol into (4).

The calculated mass scattering and backscattering efficiencies averaged over latitudinal regions of the Pacific from RITS 93 and RITS 94 are shown in Table 3. For RITS 93 the weighted average and standard error from the regression of $\alpha_{sp,SO_4,ion}$ for all samples were 5.1 ± 0.21 m^2 g^{-1} and for RITS 94, 3.8 ± 0.35 m^2 g^{-1}. Values were relatively constant over all latitudinal

regions with weighted averages ranging from 4.3 to 7.5 m^2 g^{-1}. The stability of the values is a reflection of the narrow range of D_{gn} and σ_{sg} measured throughout both cruises (see Table 4). More variability in $\alpha_{sp,SO_4,ion}$ is expected in instances where D_{gn} and σ_{sg} for the nss $SO_4^=$ aerosol component vary in space or time (see, for example, *Zhang et al.* [1994]). The largest values were observed in the northern hemisphere high latitudes (40°N to 55°N) and in marine air masses in the southern and northern hemisphere midlatitudes (40°S to 20°S and 20°N to 40°N). Lowest values were found in the tropics between 20°S and 20°N.

The average and standard deviation of $\alpha_{bsp,SO_4,ion}$ was about an order of magnitude lower and displayed less variability than the scattering efficiency values. The weighted average and standard error of all RITS 93 samples were 0.43 ± 0.02 m^2 g^{-1} and for RITS 94, 0.40 ± 0.03 m^2 g^{-1}. Weighted averages ranged from 0.41 to 0.58 m^2 g^{-1} over all latitudinal regions. The lower degree of variability in the backscattering efficiencies compared to the scattering efficiencies is a result of a weaker dependence of σ_{bsp} than σ_{sp} on particle size for diameters between 0.2 and 1.0 µm [*Marshall*, 1994].

The weighted average and standard error of $\alpha_{sp,sub,seasalt}$ for RITS 93 were 5.0 ± 0.27 m^2 g^{-1} and for RITS 94, 4.9 ± 0.24 m^2 g^{-1}. Values of $\alpha_{bsp,sub,seasalt}$ for RITS 93 averaged 0.47 $\pm$ 0.03 m^2 g^{-1} and for RITS 94 averaged 0.42 ± 0.02 m^2 g^{-1}. The equivalent values for $\alpha_{sp,SO_4,ion}$ and $\alpha_{sp,sub,seasalt}$ as well as $\alpha_{bsp,SO_4,ion}$ and $\alpha_{bsp,sub,seasalt}$ indicate that if the submicron masses of sea salt and nss $SO_4^=$ are comparable, the contribution by submicron sea salt to scattering and backscattering by the aerosol as a whole cannot be neglected given that the submicron sea salt and nss $SO_4^=$ aerosol have similar lifetimes in the atmosphere.

Mass scattering and backscattering efficiencies for the supermicron sea-salt component were appreciably lower, however, as it is in a size range where particle scattering in the visible is less efficient per unit volume. RITS 93 and RITS 94 values of $\alpha_{sp,sup,seasalt}$ averaged 0.88 ± 0.05 m^2 g^{-1} and 0.92 $\pm$ 0.07 m^2 g^{-1}, respectively. RITS 93 and RITS 94 values of $\alpha_{bsp,sup,seasalt}$ averaged 0.08 ± 0.01 m^2 g^{-1} and 0.09 ± 0.01 m^2 g^{-1}, respectively. The lack of variability in the scattering and backscattering efficiencies of the sea-salt aerosol suggests that

Table 3. Comparison of Mass Scattering and Backscattering Efficiencies for Individual Aerosol Components and Backscattered Fraction for Aerosol at 30% RH for Latitudinal Regions of the Pacific

Site	Number of Samples	$\alpha_{sp,SO_4,ion}$[a] $(\alpha_{bsp,SO_4,ion})$ $m^2\,g^{-1}$	$\alpha_{sp,sub,seasalt}$[a] $(\alpha_{bsp,sub,seasalt})$ $m^2\,g^{-1}$	$\alpha_{sp,sup,seasalt}$[a] $(\alpha_{bsp,sup,seasalt})$ $m^2\,g^{-1}$	b[b]	Reference
NH high-latitude Pacific[c] RITS 93 and 94	5	7.4 ± 2.1 (0.47 ± 0.32)	3.5 ± 0.62 (0.33 ± 0.09)	1.1 ± 0.14 (0.11 ± 0.02)	0.094 ± 0.002	this work
NH midlatitude Pacific[d] RITS 93 (continental)	4	5.2 ± 0.72 (0.41 ± 0.02)	3.8 ± 0.42 (0.33 ± 0.004)	0.91 ± 0.05 (0.09 ± 0.01)	0.092 ± 0.001	this work
SH/NH midlatitude Pacific[e] RITS 93 and 94 (marine)	10	7.5 ± 1.7 (0.58 ± 0.13)	7.7 ± 1.6 (0.63 ± 0.13)	0.39 ± 0.25 (0.05 ± 0.02)	0.094 ± 0.004	this work
NH northeastern Pacific[f] PSI 91	7	4.2 ± 0.48 (0.46 ± 0.15)	3.7 ± 0.38 (0.43 ± 0.12)	0.90 ± 0.07 (0.11 ± 0.03)	0.1 ± 0.006	*Quinn et al.* [1995]
Tropical Pacific[g] RITS 93 and 94	22	4.3 ± 0.37 (0.43 ± 0.03)	4.2 ± 0.54 (0.41 ± 0.05)	1.1 ± 0.09 (0.09 ± 0.01)	0.097 ± 0.003	this work
Tropical Pacific[g] MAGE 92	6	6.0 ± 1.8 (0.42 ± 0.09)	3.8 ± 0.49 (0.33 ± 0.01)	0.88 ± 0.04 (0.09 ± 0.01)	0.092 ± 0.01	*Quinn et al.* [1995]
SH high-latitude Pacific[h] RITS 93 and 94	20	5.1 ± 0.43 (0.41 ± 0.05)	5.5 ± 0.22 (0.49 ± 0.03)	0.68 ± 0.08 (0.06 ± 0.01)	0.094 ± 0.003	this work

[a]Derived from equation (4).
[b]Calculated from Mie theory and based on the measured number and mass-size distributions.
[c]40°N to 55°N.
[d]20°N to 40°N, derived from the ratio of component-calculated scattering to component mass.
[e]40°S to 20°S, 20°N to 40°N.
[f]48°N, 127°W.
[g]20°S to 20°N.
[h]68°S to 40°S.

Table 4. Comparison of Accumulation Mode D_{gn} and σ_{sg} for Marine and Continental Locations

Site	D_{gn}, µm	σ_{sg}	Reference
NH high-latitude Pacific[a] RITS 93 and 94	0.18	1.44	this work
NH midlatitude Pacific[b] continental air mass RITS 93	0.21	1.38	this work
NH midlatitude Pacific[b] marine air mass RITS 94	0.17	1.41	this work
NH northeastern Pacific[c] PSI 91	0.19	1.4	*Quinn et al.* [1995]
Tropical Pacific[d] RITS 93 and 94, MAGE 92	0.19	1.41	this work; *Quinn et al.* [1995]
SH midlatitude Pacific[e] RITS 93 and 94	0.18	1.46	this work
SH high-latitude Pacific[f] RITS 93 and 94	0.15	1.54	this work
Remote ocean	0.174	1.53	*Meszaros and Vissy* [1974]
Ny Alesund, Svalbard[g]	0.22	1.4	*Covert and Heintzenberg* [1993]
Background continental[h]	0.076	2.0	*Whitby and Sverdrup* [1980]
Urban average[h]	0.054	2.16	*Whitby and Sverdrup* [1980]
Power plant plume[h]	0.061	1.83	*Cantrell and Whitby* [1978]

[a]40°N to 55°N.
[b]20°N to 40°N.
[c]48°N, 127°W.
[d]20°S to 20°N.
[e]40°S to 20°S.
[f]68°S to 40°S.
[g]79°N, 12°E.
[h]California.

the sea salt was sampled close to its source; its size distribution did not vary significantly from sample to sample (see Figure 6); and it did not undergo much alteration via gas phase absorption, cloud processing, or removal prior to being sampled.

4. Comparison of Climate Relevant Parameters Derived From RITS 93 and RITS 94 With Previously Reported Marine Values

Determining ΔF_R for tropospheric aerosols requires knowing how perturbations to the natural aerosol system through the addition of anthropogenic aerosol changes the chemical, physical, and radiative properties of the natural aerosol. These properties include the number distribution of the aerosol as a whole, the amount of light that is scattered in the upward direction by the aerosol as a whole, and the mass scattering and backscattering efficiencies of each aerosol component (natural and anthropogenic) present. Several recent cruises in the Pacific Ocean have allowed for a compilation of these quantities for aerosol in the marine atmosphere.

Geometric number mean diameters, D_{gn}, and standard deviations, σ_{sg}, for different regions of the Pacific and a selection of continental locations are listed in Table 4. Values of D_{gn} and σ_{sg} from marine air masses cover a narrow range from 0.15 to 0.19 and 1.4 to 1.54, respectively. Continentally influenced marine air masses (northern hemisphere midlatitude Pacific during RITS 93) and remote continental air masses (Ny Alesund) have slightly larger values of D_{gn} (0.21 and 0.22) but similar standard deviations (1.38 and 1.4). These values of D_{gn} indicate that the sampled marine and remote continental aerosol had undergone some degree of aging and relatively rapid growth to the Aitken mode since production. The narrow values of σ_{sg} suggest, however, that the number and variability of growth mechanisms to the accumulation size was limited. Nonremote continental air masses from California have much smaller geometric number mean diameters of 0.054 to 0.076 but larger standard deviations of about 2.0. These values are indicative of an aerosol that is close to its source. The growth that has occurred, however, has been a result of a number of mechanisms.

Values of the backscattered fraction, b, for different regions of the Pacific derived from measurements during RITS 93, RITS 94, MAGE 92, and the Pacific Sulfur Stratus Investigation (PSI 91) are compared in Table 3. Values are consistent for the four cruises, covering a narrow range from 0.092 to 0.1. This consistency is a result of the relative stability of the shape (but not necessarily magnitude) of the accumulation mode and suggests that only a limited number of aerosol production and growth mechanisms occur in the marine atmosphere. The relatively narrow range of values observed for D_{gn} and σ_{sg} in marine air masses confirms this stability.

Mass scattering and backscattering efficiencies for nss $SO_4^=$, submicron sea salt, and supermicron sea salt at 30% RH for these four cruises also are shown in Table 3. Values for all of the cruises were estimated from a multiple linear regression of the Mie-calculated scattering by the aerosol as a whole against the aerosol component masses (equation (4)). The mass scattering efficiencies for all three components are consistent among the four cruises. Average values of $\alpha_{sp,SO_4,ion}$ range from 4.2 to 7.5 m^2 g^{-1}, $\alpha_{sp,sub,seasalt}$ from 3.5 to 7.7 m^2 g^{-1}, and $\alpha_{sp,sup,seasalt}$ from 0.68 to 1.1 m^2 g^{-1}. Mass backscattering efficiencies of $\alpha_{bsp,SO_4,ion}$ range from 0.41 to 0.58 m^2 g^{-1}, $\alpha_{bsp,sub,seasalt}$ from 0.33 to 0.63 m^2 g^{-1}, and $\alpha_{bsp,sup,seasalt}$ from 0.05 to 0.11 m^2 g^{-1}.

Many values of mass scattering efficiencies for sulfate aerosol have been reported for continental regions. These include 2.0 to 6.0 m^2 g^{-1} from the Grand Canyon [Zhang et al., 1994; Anderson et al., 1994], 8 m^2 g^{-1} from Denver [Sloane et al., 1991], 5 m^2 g^{-1} from southern Sweden [Waggoner et al., 1976], 11 m^2 g^{-1} from the Canadian Arctic [Barrie and Hoff, 1985], and 12 m^2 g^{-1} from the northeastern United States [ten Brink et al., 1987]. A direct comparison of these numbers with each other and with the marine values reported here is difficult, however, because of the lack of a standard definition of the sulfate mass scattering efficiency.

The values of sulfate mass scattering efficiencies from this work are weighted averages based on Mie-calculated scattering by the aerosol as a whole and the mass concentration of the aerosol components. This calculation preserves the size resolution of the measured number distribution and takes into account the nss $SO_4^=$ size distribution. Zhang et al. [1994] use Mie-calculated ammonium sulfate scattering based on measured chemical mass distributions to estimate the sulfate mass scattering efficiency. Values from this work and from Zhang et al. [1994] assume that the aerosol is an external mixture. Sloane et al. [1991] derive sulfate scattering efficiencies in a similar manner but with models which assume either an externally or an internally mixed aerosol. These results indicate that the assumption of an external mixture yields scattering efficiencies 15 to 30% lower than if an internal mixture is assumed. In each of these methods it is assumed that only those chemical species that were analytically measured contributed to scattering by the total aerosol. If other species which also contribute to scattering are present, then the sulfate mass scattering efficiencies will be artificially high.

Values of sulfate mass scattering efficiencies reported by ten Brink et al. [1987], Waggoner et al. [1976], and Barrie and Hoff [1985] are based on the measured light scattering by the total aerosol divided by the measured mass concentration of the nss $SO_4^=$ ion. This method does not take into account the size distribution of the sulfate aerosol component. In addition, the sulfate scattering efficiencies will be overestimated if aerosol components other than nss $SO_4^=$ are present and are contributing to measured scattering by the total aerosol.

Reported values of sulfate mass scattering efficiencies also will be affected by the spectral response of the nephelometer light source, light filter, and detector phototube. Differences in this response are difficult to quantify, however, as they are a function of the number distribution which can vary greatly between different types of air masses. Ruby and Waggoner [1981] have estimated, for example, that differences in the spectral response of the Meteorology Research, Inc. (MRI) nephelometer models 1550 and 1560/90 can result in light scattering coefficients that differ by 6 to 26% depending on the size distribution.

Differences in the relative humidity of the scattering measurement also can lead to variability in reported sulfate scattering efficiencies. This effect is variable as it depends on the deliquescence properties of the nss $SO_4^=$ aerosol which, in turn, depend on the degree of neutralization of the sulfate by ammonium. Changes in ambient RH from 60 to 90% have been found to affect sulfate scattering efficiencies by as much as a factor of 2 to 3 [Weiss et al., 1982; ten Brink et al., 1987; Zhang et al., 1994]. As a result, scattering efficiencies will vary greatly if derived from nephelometer measurements of a dried airstream versus one at the ambient RH. One other factor affecting the magnitude of the sulfate scattering efficiency is the size fraction

of the nss $SO_4^=$ mass that is included in the calculation. If there is a significant amount of supermicron nss $SO_4^=$ mass, using a combined submicron and supermicron value will give a considerably different value than using only a submicron value as the two size ranges have different scattering characteristics.

On the basis of the above discussion it is difficult to determine how much of the variability in reported values of sulfate scattering efficiencies is due to differences in aerosol properties versus how much is due to differences in measurement and calculation methods. For the purpose of modeling the climatic effect of tropospheric aerosol on a global scale, a large database of scattering and nss $SO_4^=$ mass distribution measurements is needed to indicate regional and temporal variability in the sulfate scattering efficiency. Such a database must rely on a standardized method for estimating the sulfate scattering efficiency so that variability due to methods is minimized. Extending this standardization to the determination of the mass scattering efficiency for all aerosol components that contribute to scattering by the total aerosol would be very useful in determining the roles of different aerosol types in the climatic effect of tropospheric aerosol.

5. Conclusions

Presented here are data from two long latitudinal cruises in the Pacific Ocean which allow for the determination of the effect of air mass sources and synoptic scale meteorology on the chemical, physical, and optical properties of individual aerosol components. These empirical relationships are needed to assess the perturbation of the radiative properties of the natural aerosol system by the addition of anthropogenic aerosol and to incorporate the direct climate forcing by tropospheric aerosol into global climate models.

Frequent occurrence of frontal passages and the resulting subsidence of air from the free troposphere in the high latitudes (>45°) of the northern and southern hemispheres led to short marine boundary layer residence times of less than 3 days. Subsidence and transport also occurred on the edges of high-pressure systems in the midlatitudes (20° to 40°), yielding variable boundary layer residence times of 1 to 5 days. A tropical depression between midlatitude highs (20°S to 20°N) resulted in long boundary layer residence times of up to 7 days. Subsidence and short boundary layer residence times corresponded to high Aitken mode number concentrations and low accumulation mode number and nss $SO_4^=$ mass concentrations. Alternatively, long boundary layer residence times allowed for growth of the aerosol from the Aitken to the accumulation mode size range and resulted in a less prominent Aitken mode and high accumulation mode number and nss $SO_4^=$ mass concentrations.

In all regions, high Na^+ concentrations corresponded to high wind speeds, indicating the wind-driven production of sea-salt aerosols. The nss $SO_4^=$ and Na^+ masses were clearly separated into submicron and supermicron particle size fractions, respectively, with a separation geometric diameter of 0.5 μm (0.7-μm aerodynamic diameter) for the aerosol at 30% RH. As shown in Figure 1, the minimum between the two modes for the marine case requires an aerodynamic size cut ranging between 0.7 to 1.0 μm to separate the two modes.

Submicron nss $SO_4^=$ aerosol made up 35 to 40% of the submicron ionic mass and 6% of the total ionic mass. Supermicron nss $SO_4^=$ aerosol contributed only 1% to the total ionic mass. Mass fractions of nss $SO_4^=$ aerosol were highest in regions having the longest marine boundary layer residence times (the

tropics) or the largest potential sources of sulfate aerosol (>65°S where atmospheric DMS concentrations were high and the northern hemisphere midlatitudes where air was advected from North America). Mass fractions of submicron sea-salt aerosol were similar to those of submicron nss $SO_4^=$.

The latitudinal distribution of nss $SO_4^=$ light scattering followed that of the nss $SO_4^=$ mass fraction but was amplified due to the concentration of the sulfate aerosol in the accumulation mode where the scattering coefficient per unit aerosol volume is highest. Largest values were found in the high southern latitudes (up to 38% of the scattering by the total aerosol), in the tropics (up to 48%), and in the northern hemisphere between 27°N and 38°N (up to 65%). Values of the submicron sea-salt light scattering were similar to those of the sulfate aerosol. Supermicron sea-salt aerosol made up 80% of the total ionic mass but only contributed about 45% to the scattering by the total aerosol due to the low scattering coefficient at visible wavelengths per unit aerosol volume in this size range. In addition, scattering by supermicron sea-salt aerosols will only be important at low altitudes as particles of this size generally are confined to the lowest layer of the atmosphere due to their large sedimentation velocities.

Mass scattering and backscattering efficiencies for the nss $SO_4^=$ ion ranged from 4.3 to 7.5 and from 0.41 to 0.58 $m^2\ g^{-1}$, respectively. Scattering and backscattering efficiencies for submicron sea salt ranged from 3.5 to 7.7 and from 0.33 to 0.63 $m^2\ g^{-1}$, respectively. The similarity of the scattering efficiencies for sulfate and submicron sea salt indicates that the contribution by submicron sea salt to scattering by the total aerosol cannot be neglected for cases where the mass concentrations of the two components are similar. Mass scattering efficiencies of supermicron sea salt were considerably lower.

A direct comparison of the mass scattering efficiencies for the nss $SO_4^=$ ion presented here to those reported for more continental regions is difficult because of differences in the methods used for the estimation. Variability in sulfate mass scattering efficiencies can result from natural variability in aerosol properties but also can be due to the use of Mie-calculated scattering versus total measured scattering, differences in the spectral responses of the nephelometers used for the scattering measurement, differences in the measurement RH, and the use of different size fractions of the nss $SO_4^=$ ion. A standardized protocol for the determination of sulfate mass scattering efficiencies is needed to eliminate variability due to measurement methods. Given this standardized method, a global database of sulfate scattering efficiencies indicating the regional and temporal variability of sulfate aerosol properties can be developed to incorporate the direct effect of aerosols into climate models.

Values of the backscattered fraction, b, were comparable to previously reported marine values ranging from 0.092 to 0.1. This consistency is a result of stability in the shape of the accumulation mode over different latitudinal and aerosol source regions. The narrow range of values observed for D_{gn} (0.15 to 0.21 μm) and σ_{sg} (1.38 to 1.54) confirms this stability.

The data presented here consider the mass fractions and light scattering of two aerosol components, nss $SO_4^=$ and sea-salt aerosol. To determine how anthropogenic perturbations to the natural aerosol system change the radiative properties of the aerosol, this analysis should be extended to all optically relevant aerosol components, including nss $SO_4^=$, sea salt, organic carbon, elemental carbon, and mineral aerosol.

tion, and T. Anderson and R. Charlson for helpful comments. This research was funded by the Ecology and Atmospheric Chemistry Branch of the NASA Mission to Planet Earth Science Division and by the Aerosol Component of the NOAA Climate and Global Change Program. It is a contribution to the International Global Atmospheric Chemistry (IGAC) Core Project of the International Geosphere-Biosphere Programme (IGBP). This is NOAA PMEL contribution 1645 and JISAO contribution 326.

References

Anderson, T. L., R. J. Charlson, W. H. White, and P. H. McMurry, Comment on "Light scattering and cloud condensation nucleus activity of sulfate aerosol measured over the Northeast Atlantic Ocean" by D. A. Hegg et al., *J. Geophys. Res., 99*, 25,947–25,949, 1994.

Andreae, M. O., The ocean as a source of atmospheric sulfur compounds, in *The Role of Air-Sea Exchange in Geochemical Cycling*, edited by P. Buat-Menard, pp. 331–362, D. Reidel, Norwell, Mass., 1986.

Baron, P. A., Calibration and use of the aerodynamic particle sizer (APS 3300), *Aerosol Sci. Technol., 5*, 55–67, 1986.

Barrie, L. A., and R. M. Hoff, Five years of air chemistry observations in the Canadian Arctic, *Atmos. Environ., 19*, 1995–2010, 1985.

Bates, T. S., J. D. Cline, R. H. Gammon, and S. R. Kelly-Hansen, Regional and seasonal variations in the flux of oceanic dimethylsulfide to the atmosphere, *J. Geophys. Res., 92*, 2930–2938, 1987.

Bates, T. S., K. C. Kelly, J. E. Johnson, and R. H. Gammon, Regional and seasonal variations in the flux of oceanic carbon monoxide to the atmosphere, *J. Geophys. Res., 100*, 23,093–23,101, 1995.

Berner, A., C. Lurzer, F. Pohl, O. Preining, and P. Wagner, The size distribution of the urban aerosol in Vienna, *Sci. Total Environ., 13*, 245–261, 1979.

Bodhaine, B. A., N. C. Ahlquist, and R. C. Schnell, Three-wavelength nephelometer suitable for aircraft measurement of background aerosol scattering coefficient, *Atmos. Environ., 25A*, 2267–2276, 1991.

Bohren, C. F., and D. R. Huffman, *Absorption and Scattering of Light by Small Particles*, John Wiley, New York, 1983.

Bray, W. H., Water vapor pressure control with aqueous solutions of sulfuric acid, *J. Mater., 5*, 233–248, 1970.

Cantrell, B. K., and K. T. Whitby, Aerosol size distributions and aerosol volume formation for a coal-fired power plant plume, *Atmos. Environ., 12*, 323–333, 1978.

Clarke, A. D., Atmospheric nuclei in the Pacific midtroposphere: Their nature, concentration, and evolution, *J. Geophys. Res., 98*, 20,633–20,647, 1993.

Covert, D. S., and J. Heintzenberg, Size distributions and chemical properties of aerosol at Ny Alesund, Svalbard, *Atmos. Environ., 27A*, 2989–2997, 1993.

Covert, D. S., V. N. Kapustin, T. S. Bates, and P. K. Quinn, Physical properties of marine boundary layer aerosol particles of the mid-Pacific in relation to sources and meteorological transport, *J. Geophys. Res.*, in press, 1995.

Draxler, R. R., Hybrid single-particle Lagrangian integrated trajectories (HY-SPLIT): Version 3.0, User's Guide and Model Description, *Tech. Rep. ERL ARL-195*, Natl. Oceanic and Atmos. Admin., Silver Springs, Md., 1992.

Hegg, D. A., D. S. Covert, and V. N. Kapustin, Modeling a case of particle nucleation in the marine boundary layer, *J. Geophys. Res., 97*, 9851–9857, 1992.

Holland, H. D., *The Chemistry of the Atmosphere and Oceans*, p. 154, John Wiley, New York, 1978.

Hoppel, W. A., G. M. Frick, J. W. Fitzgerald, and R. E. Larson, Marine boundary layer measurements of new particle formation and the effect which nonprecipitating clouds have on the aerosol size distribution, *J. Geophys. Res., 99*, 14,443–14,459, 1994.

Keady, P. B., F. R. Quant, and G. S. Sem, Differential mobility particle sizer: A new instrument for high resolution aerosol size distribution measurements below 1 μm, *TSI Q., 9*, 3–11, 1983.

Kent, G. S., et al., Modeling atmospheric aerosol backscatter at CO_2 laser wavelengths, 1, Aerosol properties, modeling techniques, and associated problems, *Appl. Opt., 22*, 1655–1665, 1983.

Langner, J. and H. Rodhe, A global three-dimensional model of the tropospheric sulfur cycle, *J. Atmos. Chem., 13*, 225–263, 1991.

Liu, B. Y. H., and K. W. Lee, Efficiency of membrane and Nuclepore filters for submicrometer aerosols, *Environ. Sci. Technol., 10*, 345–350, 1976.

Liu, B. Y. H., and D. Pui, On the performance of the electrical aerosol analyzer, *J. Aerosol Sci., 6*, 249–264, 1975.

Marshall, S. F., Measurement-derived radiative transfer parameters for the aerosol climate forcing problem, M.S. dissertation, Univ. of Washington, Seattle, 1994.

Meszaros, A., and K. Vissy, Concentrations, size distribution and chemical nature of atmospheric aerosol particles in remote ocean areas, *J. Aerosol Sci., 5*, 101–109, 1974.

McInnes, L. M. , D. S. Covert, and B. M. Baker, The number of sea-salt sulfate and carbonaceous particles in the marine atmosphere: Measurements consistent with the ambient size distribution, in preparation, 1995a.

McInnes, L. M., P. K. Quinn, D. S. Covert, and T. L. Anderson, Gravimetric analysis, ionic composition, and associated water mass of the marine aerosol, *Atmos. Environ.*, in press, 1995b.

Merrill, J., E. Arnold, M. Leinen, and C. Weaver, Mineralogy of aeolian dust reaching the North Pacific Ocean, 2, Relationship of mineral assemblages to atmospheric transport patterns, *J. Geophys. Res., 99*, 21,025–21,032, 1994.

Monahan, E. C., The ocean as a source for atmospheric particles, in *The Role of Air-Sea Exchange in Geochemical Cycling*, edited by P. Buat-Menard, pp. 331–362, D. Reidel, Norwell, Mass., 1986.

O'Dowd, C. D., and M. H. Smith, Physicochemical properties of aerosols over the North Atlantic: Evidence for wind-speed-related submicron sea-salt aerosol production, *J. Geophys. Res., 98*, 1137–1149, 1993.

Plass-Dulmer, C., R. Koppmann, M. Ratte, and J. Rudolph, Light nonmethane hydrocarbons in seawater, *Global Biogeochem. Cycles, 9*, 79–100, 1995.

Pszenny, A. A. P., A. J. Castelle, R. A. Duce, and J. N. Galloway, A study of the sulfur cycle in the Antarctic marine boundary layer, *J. Geophys. Res., 94*, 9818–9830, 1989.

Quinn, P. K., T. S. Bates, J. E. Johnson, D. S. Covert, and R. J. Charlson, Interactions between sulfur and reduced nitrogen cycles over the central Pacific Ocean, *J. Geophys. Res., 95*, 16,405–16,416, 1990.

Quinn, P. K., D. S. Covert, T. S. Bates, V. N. Kapustin, D. C. Ramsey-Bell, and L. M. McInnes, Dimethylsulfide/cloud condensation nuclei/climate system: Relevant size-resolved measurements of the chemical and physical properties of atmospheric aerosol particles, *J. Geophys. Res., 98*, 10,411–10,427, 1993.

Quinn, P. K., S. F. Marshall, T. S. Bates, D. S. Covert, and V. N. Kapustin, Comparison of measured and calculated aerosol properties relevant to the direct radiative forcing of tropospheric sulfate aerosol on climate, *J. Geophys. Res., 100*, 8977–8992, 1995.

Rau, J. A., and M. A. K. Khalil, Anthropogenic contributions to the carbonaceous content of aerosols over the Pacific Ocean, *Atmos. Environ., 27A*, 1297–1307, 1993.

Reineking, A., and J. Porstendorfer, Measurements of particle loss functions in a differential mobility analyzer for different flow rates, *Aerosol Sci. Technol., 5*, 483–487, 1986.

Ruby, M. G., and A. P. Waggoner, Intercomparison of integrating

nephelometer measurements, *Environ. Sci. Technol.*, *15*, 109–113, 1981.

Savoie, D. L., and J. M. Prospero, Particle size distribution of nitrate and sulfate in the marine atmosphere, *Geophys. Res. Lett.*, *9*, 1207–1210, 1982.

Sloane, C. S., J. Watson, J. Chow, L. Pritchett, and L. W. Richards, Size-segregated fine particle measurements by chemical species and their impact on visibility impairment in Denver, *Atmos. Environ.*, *25A*, 1013–1024, 1991.

Stelson, A. W., Urban aerosol refractive index prediction by partial molar refraction approach, *Environ. Sci. Tech.*, *24*, 1676–1679, 1990.

Stoiber, R. E., S. N. Williams, and B. Heubert, Annual contribution of sulfur dioxide to the atmosphere by volcanos, *J. Volcanol. Geotherm. Res.*, *33*, 1–8, 1987.

Tang, I. N., and H. R. Munkelwitz, Simultaneous determination of refractive index and density of an evaporating aqueous solution droplet, *Aerosol. Sci. Technol.*, *15*, 201–207, 1991.

Tang, I. N., and H. R. Munkelwitz, Water activities, densities, and refractive indices of aqueous sulfate and nitrate droplets of atmospheric importance, *J. Geophys. Res.*, *99*, 18,801–18,808, 1994.

ten Brink, H. M., S. E. Schwartz, and P. H. Daum, Efficient scavenging of aerosol sulfate by liquid-water clouds, *Atmos. Environ.*, *21*, 2035–2052, 1987.

Waggoner, A. P., A. J. Vanderpol, R. J. Charlson, S. Larsen, L. Granat, and C. Tradgard, Sulfate light scattering ratio as an index of the role of sulfur in the tropospheric optics, *Nature*, *261*, 120–122, 1976.

Weiss, R. E., T. V. Larson, and A. P. Waggoner, In situ rapid-response measurements of $H_2SO_4/(NH_4)_2SO_4$ aerosols in rural Virginia, *Environ. Sci. Technol.*, *16*, 525–532, 1982.

Whitby, K. T., The physical characteristics of sulfur aerosols, *Atmos. Environ.*, *12*, 135–159, 1978.

Whitby, K. T., and G. M. Sverdrup, California aerosols: Their physical and chemical characteristics, *Adv. Environ. Sci. Technol.*, *10*, 477–517, 1980.

Zang, Z., and B. Y. H. Liu, Performance of TSI 3760 condensation nuclei counter at reduced pressures and flow rates, *Aerosol Sci. Technol.*, *15*, 228–238, 1991.

Zhang, X., B. J. Turpin, P. H. McMurry, S. V. Hering, and M. R. Stolzenburg, Mie theory evaluation of species contributions to 1990 wintertime visibility reduction in the Grand Canyon, *J. Air Waste Manage. Assoc.*, *44*, 153–162, 1994.

T. S. Bates, V. N. Kapustin, P. K. Quinn (corresponding author), NOAA Pacific Marine Environmental Laboratory, 7600 Sand Point Way N.E., Seattle, WA, 98115. (bates@pmel.noaa.gov; kapustin@pmel.noaa.gov; quinn@pmel.noaa.gov)

D. S. Covert, Department of Atmospheric Sciences, University of Washington, Seattle, WA 98195. (dcovert@u.washington.edu)